Baek *et al. Adv. Model. and Simul. in Eng. Sci.* (2022) 9:20
https://doi.org/10.1186/s40323-022-00233-9

Advanced Modeling and Simulation in Engineering Sciences

RESEARCH ARTICLE Open Access

A deformation-dependent coupled Lagrangian/semi-Lagrangian meshfree hydromechanical formulation for landslide modeling

Jonghyuk Baek[1], Ryan T. Schlinkman[1], Frank N. Beckwith[2] and Jiun-Shyan Chen[1*]

*Correspondence:
js-chen@ucsd.edu

[1] Department of Structural Engineering, University of California San Diego, La Jolla, CA, USA
[2] Sandia National Laboratories, Albuquerque, NM, USA

Abstract

The numerical modelling of natural disasters such as landslides presents several challenges for conventional mesh-based methods such as the finite element method (FEM) due to the presence of numerically challenging phenomena such as severe material deformation and fragmentation. In contrast, meshfree methods such as the reproducing kernel particle method (RKPM) possess unique features conducive to modelling extreme events such as the absence of a structured mesh and the ease of adaptive refinement, among others. While the semi-Lagrangian reproducing kernel (SL-RK) shape functions of RKPM defined in the current configuration have proven to be effective in extreme event modelling, the computational cost for the re-evaluation of the shape functions at every time step is costly. In this work, a deformation-dependent coupling of the Lagrangian reproducing kernel (L-RK) and SL-RK approximations is proposed for the solution of a hydro-mechanical formulation for effective simulations of landslides. The ramp function is constructed based on an equivalent plastic strain as a deformation-dependent transition from L-RK shape functions to SL-RK ones as the deformation progresses. The particular focus of the paper will be on modelling seepage-induced landslides with a mixed u–p formulation to couple the solid and fluid phases. Examples are presented to examine the effectiveness of this coupled Lagrangian/semi-Lagrangian reproducing kernel (L–SL RK) formulation and to highlight its performance in landslide modelling.

Keywords: Meshfree modeling, Reproducing kernel particle method, Landslide, Lagrangian semi-Lagrangian coupling

Introduction

Attempting to model disaster events presents several challenges for conventional analysis methods due to the associated extreme deformation, strain localization, damage, material instability, multi-body contact without knowing the contacting surfaces beforehand, and multi-physics coupling. Under the finite element framework, Eulerian FEM has been used to solve dam-break and landslide problems [1] by treating the landslide material like a fluid flow. While without mesh distortion, representation of

the free surface with Eulerian formulations is arduous. The coupled Eulerian–Lagrangian (CEL) method separates the solution procedure into Lagrangian and Eulerian steps and has recently been effectively used to model landslide runout and retrogression of earthquake-induced landslides [2, 3] as well as large rock avalanches and rapid dry flows [4, 5]. However, the transfer of solution variables from the Lagrangian frame of reference to the Eulerian frame might result in accumulated errors. The arbitrary Lagrangian–Eulerian (ALE) method has also been proposed to model large deformation in slope embankments [6], debris flows [7], and the impact of landslides against structures such as barriers and buildings [8–10]. While successful, ALE involves costly re-meshing to avoid mesh entanglement, and the transfer of field and state variables to new points necessitates the use of stabilization algorithms [11, 12].

The particle finite element method (PFEM) has been effectively introduced to model landslides [13] including seepage-induced landslides [14], retrogressive slope failures [15–18], submarine landslides [19], and the fluid–structure interaction of landslide-generated waves [20, 21]. PFEM keeps the nodes from one mesh to the next and simply retriangulates to get the nodal connectivity to remedy mesh distortion in the conventional Lagrangian discretization approach. While the field variables do not require remapping, state variables do, which could lead to error accumulation [22]. The material point method (MPM) is a method which bridges Lagrangian material points and an Eulerian grid and has been successfully applied to seepage-induced landslides simulations [23, 24]. To resolve cell-crossing instability, several enhancements have been proposed, such as using dual background grids with a boundary correction [25], by partitioning the material points into material subpoints on each side of a cell divide [26], and by using higher-order interpolation functions such as splines used in moving least-squares-type methods [27]. The discrete element method (DEM), which models material using discrete particles rather than a continuum, can simulate inter-particle details in particulate flows [28] granular avalanches [29], earthquake-induced landslides [30, 31], typhoon-induced landslides [32], rainfall-induced flowslides [33], and has been combined with other methods such as smoothed particle hydrodynamics (SPH) to model liquefaction of saturated granular solids [34]. Since DEM requires contact assessment between particles, it necessitates costly fine temporal discretization. SPH has been effectively applied to an assortment of problems especially involving flows or flow-like behavior such as seen in dry and seepage-induced landslides [35–38]. Recent enhancements of SPH include corrections for a lack of consistency in the approximation, numerical fracture, and inaccurate gradient estimates [39–41].

Meshfree methods such as the reproducing kernel particle method (RKPM) [42–44] circumvent issues involving mesh distortion and material fragmentation [45–48]. RKPM allows independent control of the orders of continuity and completeness in the approximation. Accordingly, it is relatively straightforward to carry out h- and p-adaptive refinement. The kernel functions can also naturally serve as contact indicators for multi-body contact problems where the contacting surfaces are not known a priori [49]. RKPM has been successfully applied to problems involving very large deformation [44, 50, 51], damage evolution [52], and impact/fragmentation processes [49, 53–55].

RKPM has been used for large deformation problems utilizing a Lagrangian description (L-RK) where the weak form equation was formulated with reference to either the

undeformed (total Lagrangian) or deformed (updated Lagrangian) configuration. The ability to map from the undeformed configuration to the deformed configuration by way of the deformation gradient meant that the computationally-intensive RK shape functions and their gradients would only have to be computed once at the beginning of the simulation [44, 50, 51]. In some severe deformation cases such as fracture or material damage where material separation occurs, however, the mapping is no longer one-to-one, and the inverse of the deformation gradient is no longer unique. In cases such as these, the updated Lagrangian formulation can be used for the weak form, and the RK shape functions and their gradients must be recomputed following the material points with updated neighbors at each time step to reflect the new free surface topology in the deformed configuration. This formulation is called semi-Lagrangian RKPM (SL-RK) [56, 57] and has been successfully applied to an array of severe deformation problems such as fracture and fragmentation [53, 54, 57, 58], earth-moving and landslides [57, 59, 60], and rock collapse and reconsolidation [61]. The major drawback to this formulation, however, is its high computational cost.

In [62], a blending of the two approaches was proposed. A semi-Lagrangian formulation is used only in those regions of the domain where severe deformations occur, and a Lagrangian formulation is used everywhere else. Like an FEM/meshfree coupling [63], the Lagrangian/semi-Lagrangian (L–SL) coupling can be accomplished using a transition zone where Lagrangian and semi-Lagrangian shape functions and their derivatives are blended through a ramp function thus guaranteeing continuity and consistency in the approximation. This coupling reduces the computational cost by limiting the regions where the RK shape functions and their gradients need to be re-calculated at each time step. As a result, it was successfully demonstrated that the L–SL coupling is efficient and accurate for severe deformation problems. Nevertheless, [62] used Lagrangian, transition, and semi-Lagrangian zones that were fixed in space. This is possible only if one knows the areas where extreme deformation (i.e., semi-Lagrangian regions) will occur beforehand.

In this work, we propose a deformation-dependent, Lagrangian/semi-Lagrangian coupled reproducing kernel (L–SL RK) approximation for use in simulations in which the regions of extreme deformation where the SL-RK approximation should be used cannot be pre-determined. This paper applies the proposed deformation-dependent coupled L–SL RK formulation for a computationally efficient and accurate hydro-mechanical simulation of seepage-induced landslides. A blending of Lagrangian and semi-Lagrangian shape functions is achieved by introducing an equivalent plastic strain-based ramp function which evolves with the regions under severe deformation. This blending guarantees continuity and consistency in the spatial approximation, and the gradual development of equivalent plastic strain yields a smooth L–SL transition in time that minimizes spurious wave generation caused by nodes suddenly switching from one approximation to the other.

In seepage-induced landslides, the failure of the porous geomaterial is tied to fluid pressure, and so, it is necessary to couple the fluid seepage physics with the equation of linear momentum of the solid. Previous researchers [23] have used an equal-order approximation for both the soil displacement as well as the fluid pore pressure. To avoid spurious pressure oscillations due to the violation of the numerical inf–sup

stability criterion in mixed formulations [64], we utilize an equal-order u-p approximation together with a fluid pressure projection method [59, 65–67].

The rest of this paper is organized as follows. In "Basic equations" section, we detail the mixed u–p approximation for the hydromechanical modelling of saturated porous media. "Reproducing kernel approximation" section reviews the reproducing kernel approximation in both its Lagrangian and semi-Lagrangian formulations. In "Coupled Lagrangian/semi-Lagrangian reproducing kernel particle method" section, we discuss the Lagrangian/semi-Lagrangian coupled formulation and the deformation-dependent blending based on equivalent plastic strain that evolves with regions under severe deformation. In "Numerical examples" section, we give numerical examples to examine the effectiveness of the L–SL coupling for modeling a 1D wave propagation in poroelastic media under challenging kernel support conditions, the collapse of a granular column, and a seepage-induced levee failure leading to landslide. Concluding remarks are given in "Conclusion" section.

Basic equations

Mechanics of the problem

Let Ω be a domain of a triphasic porous body that is represented as a continuum of an immiscible mixture of solid and water, the physical quantities of which are determined by spatial averaging. Consider $\mathbf{x} = \varphi(\mathbf{X}, t)$ to be a spatial point of solid in the current configuration mapped from the material point of solid $\mathbf{X}$ in the undeformed configuration. The solid displacement, velocity, and acceleration are defined as $\mathbf{u} = \mathbf{x} - \mathbf{X}$, $\mathbf{v} = \dot{\mathbf{u}}$, and $\mathbf{a} = \ddot{\mathbf{u}}$, respectively, where $\dot{(\cdot)}$ and $\ddot{(\cdot)}$ denote the first and second order material time derivatives, respectively. The water seepage velocity $\mathbf{q}^w$ is defined as the relative velocity of fluid with respect to the solid velocity: $\mathbf{q}^w = n^w\left(\mathbf{v}^w - \mathbf{v}\right)$ where $\mathbf{v}^w$ and n^w denote water velocity and volume fraction of water, respectively. Due to the relatively small contribution of air in the balance equations, its effect is ignored.

Balance equations

The balance of linear momentum in the deformed configuration is given as:

$$\nabla_{\mathbf{x}} \cdot \boldsymbol{\sigma} + \rho\mathbf{g} - \rho\ddot{\mathbf{u}} = 0 \tag{1}$$

where $\nabla_{\mathbf{x}}$ is the partial derivative operator with respect to the deformed configuration and $\mathbf{g}$ is the gravitational acceleration vector. The average mass density ρ is given as:

$$\rho = \left(1 - n^f\right)\rho^s + n^f S^w \rho^w \tag{2}$$

where n^f is the porosity, S^w is the water saturation, and ρ^s and ρ^w are the mass densities of the solid and water, respectively. Due to the fluid pressure, the total Cauchy stress of the solid is expressed as:

$$\boldsymbol{\sigma} = \widetilde{\boldsymbol{\sigma}} - \alpha S^w p^w \mathbf{I} \tag{3}$$

where $\widetilde{\boldsymbol{\sigma}}$ is the effective Cauchy stress, p^w is the water pressure, $\mathbf{I}$ is the second-order identity tensor, Biot's coefficient is $\alpha = 1 - K/K^s$, K and K^s are the drained bulk

modulus of the solid skeleton and solid grains, respectively. Substituting Eq. (3) into (1), we get:

$$\nabla_{\mathbf{x}} \cdot \left(\widetilde{\boldsymbol{\sigma}} - \alpha S^w p^w \mathbf{I}\right) + \rho \mathbf{g} - \rho \ddot{\mathbf{u}} = 0 \tag{4}$$

The conservation of mass for water flow is [68, 69]:

$$\alpha \nabla_{\mathbf{x}} \cdot \dot{\mathbf{u}} + \nabla_{\mathbf{x}} \cdot \mathbf{q}^w + \frac{1}{Q} \dot{p}^w = 0 \tag{5}$$

where Q is the modified compressibility modulus:

$$\frac{1}{Q} = C^s + \frac{n^f S^w}{K^w} + \frac{S^w \left(\alpha - n^f\right)\left(S^w + C^s p^w / n^f\right)}{K^s} \tag{6}$$

and $C^s = n^f \partial S^w / \partial p^w$ and K^w is the bulk modulus of water.

Along with the above equations, the strong form of the problem involves the following boundary conditions:

$$\begin{array}{ll} \mathbf{u} = \overline{\mathbf{u}} & \text{on } \Gamma_u \\ \mathbf{n}_t \cdot \boldsymbol{\sigma} = \bar{\mathbf{t}} & \text{on } \Gamma_t \\ p^w = \overline{p} & \text{on } \Gamma_p \\ \mathbf{n}_q \cdot \mathbf{q}^w = \mathbf{n}_q \cdot \overline{\mathbf{q}} & \text{on } \Gamma_q \end{array} \tag{7}$$

and the following initial conditions:

$$\mathbf{u} = \mathbf{u}_0, \quad \mathbf{v} = \mathbf{v}_0, \quad p^w = p_0, \quad \text{at } t = 0 \tag{8}$$

where $\overline{\mathbf{u}}$ is the applied displacement on the solid essential boundary Γ_u, $\bar{\mathbf{t}}$ and $\mathbf{n}_t$ are the applied effective traction and the outward normal vector on the traction boundary Γ_t, respectively, $\overline{p}$ is the applied water pressure on the water pressure boundary Γ_p, $\overline{\mathbf{q}}$ and $\mathbf{n}_q$ are the applied water seepage velocity and the outward normal on the water inflow boundary Γ_q, respectively, where $\Gamma_u \bigcup \Gamma_t = \Gamma, \Gamma_p \bigcup \Gamma_q = \Gamma, \Gamma_u \bigcap \Gamma_t = \varnothing, \Gamma_p \bigcap \Gamma_q = \varnothing$.

Constitutive laws

In this work, we adopt the Drucker–Prager plasticity model for the stress–strain relationship together with the Jaumann objective stress rate [70]. We use Darcy's law to relate the water pressure gradient $\nabla_{\mathbf{x}} p^w$ to the water seepage velocity, $\mathbf{q}^w$:

$$\mathbf{q}^w = -\mathbf{k}^w \cdot \left(\nabla_{\mathbf{x}} p^w - S^w \rho^w \mathbf{g}\right) \tag{9}$$

where $\mathbf{k}^w = \left(k^{rw} / \mu^w\right) \mathbf{k}_{in}^w$ is the permeability tensor, $\mathbf{k}_{in}^w$ is the intrinsic permeability, k^{rw} is the relative permeability to water, and μ^w is the dynamic viscosity of water. We use the van Genuchten model for hydraulic conductivity [71]:

$$S^w = S^{rw} + \left(1 - S^{rw}\right)\left[1 + \left(\frac{\beta p^w}{\gamma^w}\right)^n\right]^{-m} \tag{10}$$

$$k^{rw} = \sqrt{S_e}\left[1 - \left(1 - \sqrt[m]{S_e}\right)^m\right]^2 \tag{11}$$

where S^w is the degree of water saturation, k^{rw} is the relative permeability to water, $S_e = \left(S^w - S^{rw}\right)/\left(1 - S^{rw}\right)$ is the effective water saturation, S^{rw} is the irreducible water saturation, and n, m, and β are empirical parameters. Substituting Eq. (9) into (5), we have:

$$\alpha \nabla_{\mathbf{x}} \cdot \dot{\mathbf{u}} - \nabla_{\mathbf{x}} \cdot \left[\mathbf{k}^w \cdot \left(\nabla_{\mathbf{x}} p^w - S^w \rho^w \mathbf{g}\right)\right] + \frac{1}{Q}\dot{p}^w = 0 \tag{12}$$

Variational formulation

Let $\mathbf{u}^h$ and p^h be approximations of the solid displacement $\mathbf{u}$ and the water pressure p, respectively, and let both approximations use the reproducing kernel approximation described in detail in the following section:

$$\mathbf{u}^h = \sum_{I=1}^{NP} \Psi_I \mathbf{d}_I \tag{13}$$

$$p^h = \sum_{I=1}^{NP} \Psi_I p_I \tag{14}$$

where Ψ_I is the RK shape function of node I and $\mathbf{d}_I$ and p_I are nodal coefficients of node I. Furthermore, let $\delta\mathbf{u}^h$ and δp^h be variations of the solid displacement and water pressure approximations, respectively:

$$\delta\mathbf{u}^h = \sum_{I=1}^{NP} \Psi_I \delta\mathbf{d}_I \tag{15}$$

$$\delta p^h = \sum_{I=1}^{NP} \Psi_I \delta p_I \tag{16}$$

where $\delta\mathbf{d}_I$ and δp_I are nodal coefficients of node I. Following [67], after multiplying Eq. (4) by its test function $\delta\mathbf{u}^h$, performing integration by parts, using the divergence theorem, and rearranging, we get:

$$\begin{aligned} &\int_{\Omega_x} \delta\mathbf{u}^h \cdot \rho\ddot{\mathbf{u}}^h d\Omega + \int_{\Omega_x} \boldsymbol{\varepsilon}\left(\delta\mathbf{u}^h\right) : \widetilde{\boldsymbol{\sigma}}\left(\mathbf{u}^h\right) d\Omega - \int_{\Omega_x} \nabla_{\boldsymbol{x}} \cdot \delta\mathbf{u}^h \alpha S^w p^h d\Omega \\ &= \int_{\Omega_x} \delta\mathbf{u}^h \cdot \rho\mathbf{g} d\Omega + \int_{\Gamma_x^t} \delta\mathbf{u}^h \cdot \bar{\mathbf{t}} d\Gamma \end{aligned} \tag{17}$$

Likewise, we multiply Eq. (12) by a test function δp^h, perform integration by parts, use the divergence theorem, add a pressure projection, and rearrange:

$$\begin{aligned}
&\int_{\Omega_x} \delta p^h \alpha \nabla_{\mathbf{x}} \cdot \dot{\mathbf{u}}^h d\Omega + \int_{\Omega_x} \delta p^h Q^{-1} \dot{p}^h d\Omega \\
&+ \int_{\Omega_x} \nabla_{\mathbf{x}} \delta p^h \cdot \mathbf{k}^w \cdot \nabla_{\mathbf{x}} p^h d\Omega + \int_{\Omega_x} \varepsilon_f \left(\delta p^h - \Pi \delta p^h\right)\left(p^h - \Pi p^h\right) d\Omega \\
&= \int_{\Omega_x} \nabla_{\mathbf{x}} \delta p^h \cdot \mathbf{k}^w \cdot S^w \rho^w \mathbf{g} d\Omega + \int_{\Gamma_x^q} \delta p^h \mathbf{n}_{\mathrm{q}} \cdot \overline{\mathbf{q}} d\Gamma
\end{aligned} \tag{18}$$

where the last term on the left-hand side of Eq. (18) is a least-squares pressure projection which stabilizes the equal-order coupled approximation [59, 65–67, 72–74], and Π is a projection operator:

$$\Pi(\cdot)\Big|_{\Omega_I} = \frac{1}{V_I} \int_{\Omega_I} (\cdot) d\Omega \tag{19}$$

where ε_f is a stabilization parameter. Following [59, 67, 74], we use the following for ε_f:

$$\varepsilon_f = \left\langle 1 - 3\frac{c_v \Delta t}{(h_I)^2} \right\rangle \frac{\left[1 + \tanh\left(2 - 12\frac{c_v \Delta t}{(h_I)^2}\right)\right]}{M' \Delta t} \tag{20}$$

where $\langle \cdot \rangle$ is the Macaulay bracket, h_I is the characteristic nodal distance which is $h_I = \sqrt{V_I}$ or $h_I = \sqrt[3]{V_I}$ for two- and three-dimensional problems, respectively, $c_v = k_f M^{'}$, k_f is the permeability parameter, and $M^{'}$ is given by:

$$M' = \frac{1}{\frac{1}{Q} + \frac{\alpha^2}{K + \frac{4G}{3}}} \tag{21}$$

where Q is the modified compressibility modulus from Eq. (6), α is Biot's coefficient, K is the drained bulk modulus of the solid skeleton, and G is the drained shear modulus of the solid skeleton.

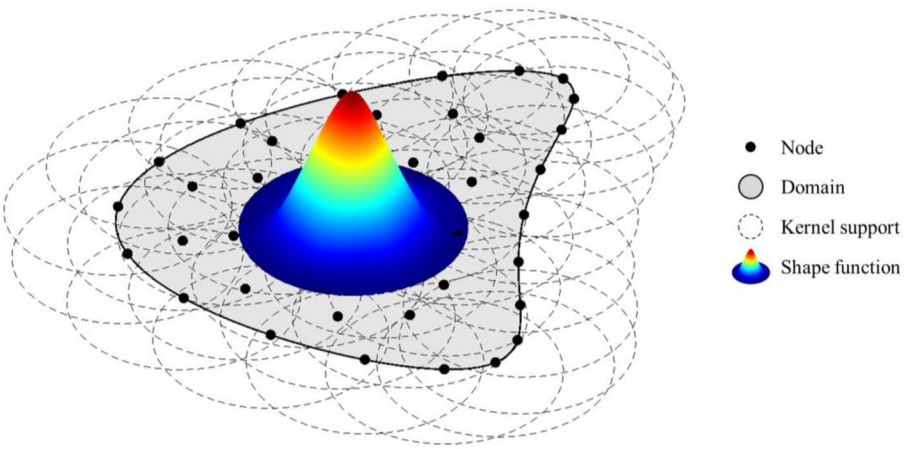

Fig. 1 A domain $\Omega_{\mathbf{X}}$ is discretized by a set of nodes. Each node has a kernel support (circular in this example) where the shape function Ψ_I is defined

Reproducing kernel approximation

Lagrangian reproducing kernel approximation

In the reproducing kernel particle method (RKPM) [42–44], the approximation $f^h(\mathbf{X})$ of a function $f(\mathbf{X})$ is based on a set of NP scattered nodes as shown in Fig. 1.

The Lagrangian reproducing kernel (L-RK) approximation is given as follows [44, 51]:

$$f^h(\mathbf{X},t) = \sum_{I=1}^{NP} \Psi_I^L(\mathbf{X}) f_I(t) \tag{22}$$

where $f^h(\mathbf{X},t)$ is the approximated function evaluated at material point $\mathbf{X}$ in the undeformed configuration, $\Psi_I^L(\mathbf{X})$ is the L-RK shape function of node I, and $f_I(t)$ is the nodal coefficient at node I. The kernel function defined on a compact support with a support size measure a, $\phi_a(\mathbf{X}-\mathbf{X}_I)$, is multiplied by a correction function, $C(\mathbf{X};\mathbf{X}-\mathbf{X}_I)$, to produce the RK shape function:

$$\Psi_I^L(\mathbf{X}) = C(\mathbf{X};\mathbf{X}-\mathbf{X}_I)\phi_a(\mathbf{X}-\mathbf{X}_I) \tag{23}$$

The correction function allows the RK approximation to exactly reproduce a polynomial field. Thus, the correction function for three-dimensional problems that reproduces nth order monomials is:

$$C(\mathbf{X};\mathbf{X}-\mathbf{X}_I) = \sum_{i+j+k=1}^{n} (X_1-X_{1I})^i (X_2-X_{2I})^j (X_3-X_{3I})^k b_{ijk}(\mathbf{X}) \equiv \mathbf{H}^T(\mathbf{X}-\mathbf{X}_I)\mathbf{b}(\mathbf{X}) \tag{24}$$

where $\mathbf{b}(\mathbf{X})$ is the vector of coefficients:

$$\mathbf{b}^T(\mathbf{X}) = [b_{000}(\mathbf{X}), b_{100}(\mathbf{X}), b_{010}(\mathbf{X}), b_{001}(\mathbf{X}), b_{200}(\mathbf{X}), \ldots, b_{00n}(\mathbf{X})] \tag{25}$$

and $\mathbf{H}(\mathbf{X}-\mathbf{X}_I)$ is the basis vector:

$$\mathbf{H}^T(\mathbf{X}-\mathbf{X}_I) = \left[1, X_1-X_{1I}, X_2-X_{2I}, X_3-X_{3I}, (X_1-X_{1I})^2, \ldots, (X_3-X_{3I})^n\right] \tag{26}$$

The order of completeness in the approximation is determined by the basis order n. For example, a linear basis will be able to reproduce a linear field exactly. The elements of $\mathbf{b}(\mathbf{X})$ are determined to meet the reproducing conditions:

$$\sum_{I=1}^{NP} \Psi_I^L(\mathbf{X}) X_{1I}^i X_{2I}^j X_{3I}^k = X_1^i X_2^j X_3^k, \ 0 \le i+j+k \le n \tag{27}$$

or equivalently:

$$\sum_{I=1}^{NP} \Psi_I^L(\mathbf{X})(X_1-X_{1I})^i (X_2-X_{2I})^j (X_3-X_{3I})^k = \delta_{i0}\delta_{j0}\delta_{k0}, 0 \le i+j+k \le n \tag{28}$$

Combining (23) and (24) and substituting into (28) we have:

$$\mathbf{b}^T(\mathbf{X})\sum_{I=1}^{NP}\mathbf{H}(\mathbf{X}-\mathbf{X}_I)\mathbf{H}^T(\mathbf{X}-\mathbf{X}_I)\phi_a(\mathbf{X}-\mathbf{X}_I)=\mathbf{H}^T(\mathbf{0}) \tag{29}$$

Solving for $\mathbf{b}(\mathbf{X})$:

$$\mathbf{b}^T(\mathbf{X})=\mathbf{H}^T(\mathbf{0})\mathbf{M}^{-1}(\mathbf{X}) \tag{30}$$

where $\mathbf{M}(\mathbf{X})$ is the moment matrix:

$$\mathbf{M}(\mathbf{X})=\sum_{I=1}^{NP}\mathbf{H}(\mathbf{X}-\mathbf{X}_I)\mathbf{H}^T(\mathbf{X}-\mathbf{X}_I)\phi_a(\mathbf{X}-\mathbf{X}_I) \tag{31}$$

For the moment matrix to be invertible, the evaluation point $\mathbf{X}$ must be covered by at least the number of non-collinear (in 2D) or non-coplanar (in 3D) kernel supports equal to the length of the basis vector [75]. Therefore, the L-RK shape function equation is given as:

$$\Psi_I^L(\mathbf{X})=\mathbf{H}^T(\mathbf{0})\mathbf{M}^{-1}(\mathbf{X})\mathbf{H}(\mathbf{X}-\mathbf{X}_I)\phi_a(\mathbf{X}-\mathbf{X}_I) \tag{32}$$

The kernel function determines the level of continuity in the approximation and is independent of the basis order. For example, the cubic B-spline kernel is C^2 continuous:

$$\phi_a(z)=\begin{cases}\frac{2}{3}-4z_I^2+4z_I^3, & 0\le z_I\le\frac{1}{2}\\ \frac{4}{3}(1-z_I)^3, & \frac{1}{2}<z_I\le 1\\ 0, & z_I>1\end{cases} \tag{33}$$

where z_I is the normalized distance in the undeformed configuration from the node with support size a_I:

$$z_I=\frac{\|\mathbf{X}-\mathbf{X}_I\|}{a_I} \tag{34}$$

Since the L-RK shape function gradients are calculated once in the undeformed configuration, using an updated Lagrangian formulation makes it necessary to update the gradients to account for large deformation. Fortunately, the L-RK shape function gradients in the current, deformed configuration may be calculated using the chain rule of differentiation [44]:

$$\nabla_{\mathbf{x}}f^h(\mathbf{X},t)=\frac{\partial f^h(\mathbf{X},t)}{\partial x_j}=\frac{\partial f^h(\mathbf{X},t)}{\partial X_i}\frac{\partial X_i}{\partial x_j}=\frac{\partial f^h(\mathbf{X},t)}{\partial X_i}F_{ij}^{-1}=\sum_{I=1}^{NP}\left[\frac{\partial\Psi_I^L(\mathbf{X})}{\partial X_i}F_{ij}^{-1}\right]f_I(t) \tag{35}$$

where $\mathbf{F}$ is the deformation gradient tensor and $\mathbf{F}^{-1}$ is obtained by direct inversion of $\mathbf{F}$. Since this transformation depends on the invertibility of the deformation gradient, updating the shape function gradients is no longer possible when the mapping from the initial, undeformed configuration to the current, deformed configuration is not one-to-one and, thus, $\mathbf{F}^{-1}$ is no longer unique. This can happen, for example, in extreme deformation problems in which material separation, fragmentation, or solid flows (as in landslides) occur.

Semi-Lagrangian reproducing kernel approximation

To circumvent the issue of a non-unique $\mathbf{F}^{-1}$ when deformation is severe, the updated Lagrangian description of material motion is used, but the shape functions and their gradients are recalculated in the current, deformed configuration. This is referred to as the semi-Lagrangian reproducing kernel (SL-RK) approximation [53, 56, 57]:

$$f^h(\mathbf{x},t) = \sum_{I=1}^{NP} \Psi_I^{SL}(\mathbf{x}) f_I(t) \tag{36}$$

where Ψ_I^{SL} is the SL-RK shape function associated with node I which is located at $\mathbf{x}_I = \varphi(\mathbf{X}_I, t)$ and evaluated at current configuration point $\mathbf{x}$. The SL-RK shape function is given as:

$$\Psi_I^{SL}(\mathbf{x}) = C(\mathbf{x}; \mathbf{x} - \mathbf{x}_I)\phi_a(\mathbf{x} - \mathbf{x}_I) \tag{37}$$

where $C(\mathbf{x}; \mathbf{x} - \mathbf{x}_I)$ and $\phi_a(\mathbf{x} - \mathbf{x}_I)$ are the semi-Lagrangian correction function and kernel function, respectively. The correction function is defined as:

$$C(\mathbf{x}; \mathbf{x} - \mathbf{x}_I) = \mathbf{H}^T(\mathbf{x} - \mathbf{x}_I)\mathbf{b}(\mathbf{x}) \tag{38}$$

where $\mathbf{H}(\mathbf{x} - \mathbf{x}_I)$ is the basis vector and $\mathbf{b}(\mathbf{x})$ is the vector of coefficients. Like the L-RK shape functions, the vector of coefficients may be solved by imposing reproducing conditions but now in the current, deformed configuration. Thus, the SL-RK shape function is given as:

$$\Psi_I^{SL}(\mathbf{x}) = \mathbf{H}^T(\mathbf{0})\mathbf{M}^{-1}(\mathbf{x})\mathbf{H}(\mathbf{x} - \mathbf{x}_I)\phi_a(\mathbf{x} - \mathbf{x}_I) \tag{39}$$

where $\mathbf{M}(\mathbf{x}) = \sum_{I=1}^{NP} \mathbf{H}(\mathbf{x} - \mathbf{x}_I)\mathbf{H}^T(\mathbf{x} - \mathbf{x}_I)\phi_a(\mathbf{x} - \mathbf{x}_I)$ is the moment matrix defined in the deformed configuration.

Figure 2 compares L-RK and SL-RK shape functions under large but not extreme deformation. Since the kernel support and the reproducing conditions of the SL-RK

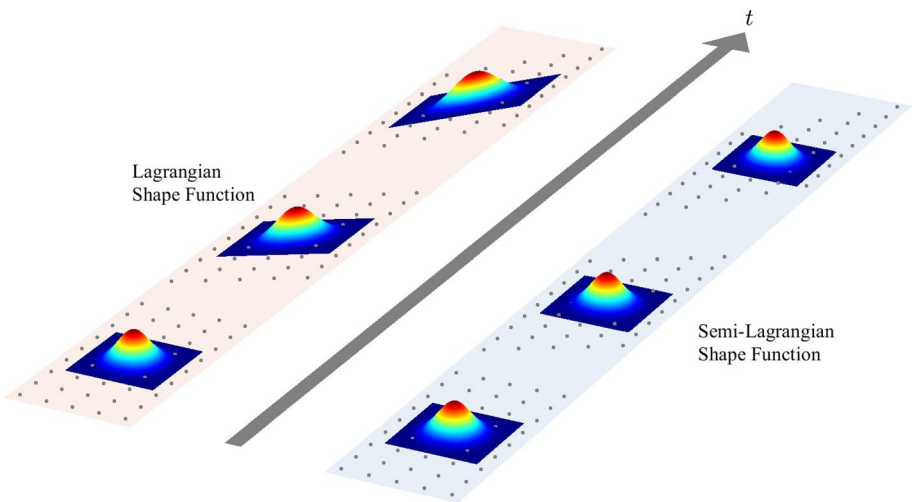

Fig. 2 Lagrangian and semi-Lagrangian shape functions under progressive deformation. The shape functions are plotted only on their kernel support. The gray points denote nodal points

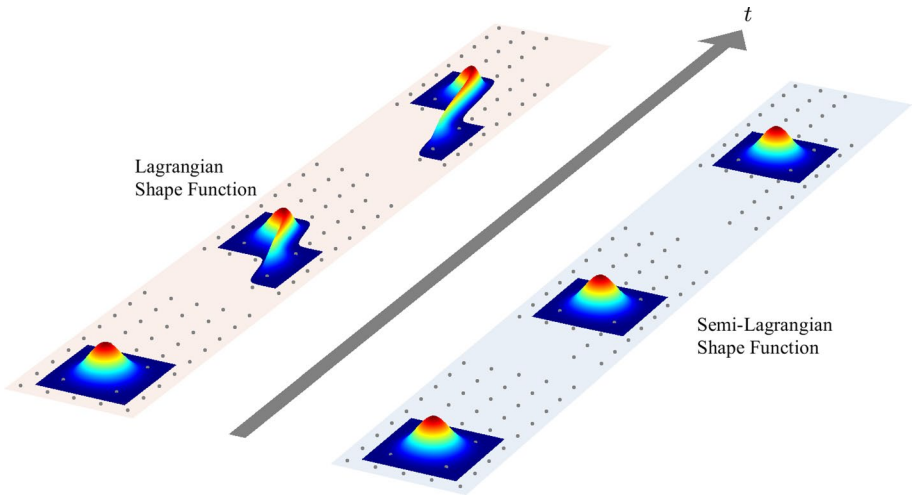

Fig. 3 Lagrangian and semi-Lagrangian shape functions under shear localization. The shape functions are plotted only on their kernel support. The gray points denote nodal points

shape function are defined in the current configuration, the support center of the SL-RK shape function follows the material motion, but the support does not attach to the material deformation. Therefore, the semi-Lagrangian kernel support can cover different sets of RK nodes at different points in time. Conversely, the support of the L-RK shape function deforms following the material deformation since the undeformed configuration is taken as the reference configuration.

Under extreme deformation, such as shear localization induced by landslides, a Lagrangian kernel support can be severely distorted, as shown in Fig. 3. Since its support is based on the initial configuration, the Lagrangian kernel support will continue to cover the same set of material points without the ability to redefine new neighboring points in the event of material fracture or fragmentation during deformation. The SL-RK shape function resolves this issue by reevaluating the neighboring points based on the current deformation state.

Because the SL-RK shape functions are calculated based on the deformed configuration, it can happen that there might not be enough nodes whose supports cover a certain evaluation point. This can occur when, for example, a single node is detached from the main body of nodes during fragmentation. To avoid having to reduce such a node's basis order to constant, the quasi-linear reproducing kernel formulation can be used [76]. On this approach, first-order polynomial reproducing conditions are approximately enforced to give a nonsingular moment matrix even when there is an insufficient number of neighbors.

Unlike the L-RK shape functions, the material time derivative of the SL-RK shape functions does not vanish since the shape functions are calculated using the moving, deformed configuration. The velocity, for instance, is given by [15]:

$$\dot{u}_i^h(\mathbf{x},t) = \sum_{I=1}^{NP} \left[\Psi_I^{SL}(\mathbf{x}) \dot{d}_{Ii}(t) + \Psi_I^{*}(\mathbf{x}) d_{Ii}(t) \right] \tag{40}$$

where $\dot{\mathbf{d}}_I$ is the generalized nodal velocity vector for node I and Ψ_I^* is the correction due to the time rate of change of the semi-Lagrangian kernel $\dot{\phi}_a$:

$$\Psi_I^*(\mathbf{x}) = C(\mathbf{x}; \mathbf{x} - \mathbf{x}_I)\dot{\phi}_a(\mathbf{x} - \mathbf{x}_I) \tag{41}$$

where:

$$\begin{aligned}\dot{\phi}_a\left(\frac{\|\mathbf{x} - \mathbf{x}_I\|}{a}\right) = \dot{\phi}_a(z_I) = \frac{\partial \phi_a(z_I)}{\partial t} = \frac{\partial \phi_a(z_I)}{\partial z_I}\frac{\partial z_I}{\partial \mathbf{x}}\frac{\partial(\mathbf{x} - \mathbf{x}_I)}{\partial t} \\ = \frac{\partial \phi_a(z_I)}{\partial z_I}\frac{\mathbf{x} - \mathbf{x}_I}{a\|\mathbf{x} - \mathbf{x}_I\|} \cdot (\mathbf{v} - \mathbf{v}_I) = \frac{\partial \phi_a(z_I)}{\partial z_I}\frac{\mathbf{n} \cdot (\mathbf{v} - \mathbf{v}_I)}{a}\end{aligned} \tag{42}$$

where $\mathbf{n} = (\mathbf{x} - \mathbf{x}_I)/\|\boldsymbol{x} - \boldsymbol{x}_I\|$ is the unit vector pointing from the evaluation point toward node I, $\mathbf{v}$ is the velocity of the material at deformed configuration point $\mathbf{x}$, and $\mathbf{v}_I$ is the velocity of node I located at $\mathbf{x}_I = \varphi(\mathbf{X}_I, t)$. It should be noted that, since the correction function is calculated in the deformed configuration to satisfy the reproducing conditions, its time derivative does not appear in Eq. (41). Furthermore, it was shown in [49] and [77] that the contribution of terms containing Ψ_I^* are negligible and may be omitted in situations where there are moderate relative changesin nodal velocities or when a nodal integration scheme such as direct nodal integration (DNI), stabilized conforming nodal integration (SCNI), or stabilized nonconforming nodal integration (SNNI) is used.

Domain integration

For modeling landslide processes, Gauss integration is inapplicable and nodal integration is a necessity. The stabilized conforming nodal integration (SCNI) [78] was developed where a smoothed gradient is calculated over the boundaries of conforming nodal cells which fulfills the integration constraint and meets linear exactness in the Galerkin approximation [78]. For linear exactness, the smoothed gradient may be calculated as:

$$\widetilde{\Psi}_{I,i}(\mathbf{x}_L) = \frac{1}{V_L}\int_{\Omega_L} \Psi_{I,i}(\mathbf{x})d\Omega = \frac{1}{V_L}\int_{\partial\Omega_L} \Psi_I(\mathbf{x})n_i(\mathbf{x})d\Gamma \tag{43}$$

where $\widetilde{\Psi}_{I,i}$ is the smoothed shape function gradient in the ith direction, $\mathbf{x}_L$ is the location of node L, V_L is the nodal representative domain volume of node L, and n_i is ith component of the outward normal on the nodal representative domain boundary $\partial\Omega_L$. Construction of the conforming cells may be done in several ways including a Voronoi diagram or Delaunay triangulation.

For extremely large deformation and fragmentation problems where $\mathbf{F}^{-1}$ is not unique, however, SCNI nodal conforming cells would have to be recomputed with each time step, a computationally infeasible task. In response to this, a non-conforming counterpart to SCNI was developed, stabilized non-conforming nodal integration (SNNI) [53, 56]. In SNNI, the nodal integration cells are constructed as either squares or circles centered on the nodes with areas the size of their conforming counterparts. The downside to SNNI is that, since the nodal cells do not conform, it no longer meets first order variational consistency and can produce solutions with sub-optimal convergence rates. To remedy this deficiency, a variationally consistent correction of SNNI (VC-SNNI) can be

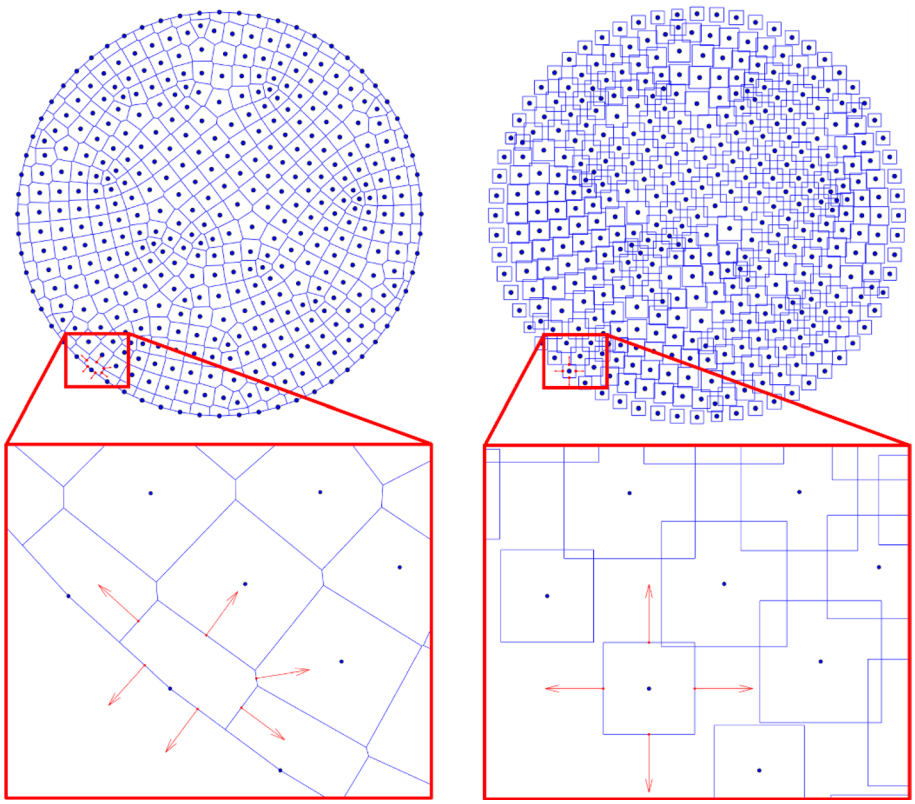

Fig. 4 Smoothed integration cells: stabilized conforming nodal integration using a Voronoi diagram (SCNI; left); stabilized non-conforming nodal integration (SNNI; right); red arrows from the cells are the outward normal vectors

considered which can achieve variational consistency to an arbitrary order [79]. Figure 4 shows a conforming discretization based on a Voronoi diagram (left) and a non-conforming discretization (right) for use with SCNI and SNNI, respectively.

Even though SCNI and VC-SNNI for the RK approximation with linear bases meet the integration constraint and first-order variational consistency, they are still nodally integrated methods, and thus reduced, integration methods. This means that they can still trigger non-physical, low-energy modes which necessitate the use of stabilization methods [80–82]. The most recent and computationally economic stabilization method is that of naturally stabilized nodal integration (NSNI) [82]. NSNI uses a Taylor series expansion of the shape function gradient matrix employing implicit gradients [83–85] for the higher-order gradient terms:

$$\widehat{\mathbf{B}}_I(\mathbf{x}_L) = \widetilde{\mathbf{B}}_I(\mathbf{x}_L) + (x - x_L) \cdot \mathbf{B}^{\nabla}_{Ix}(\mathbf{x}_L) + \left(y - y_L\right) \cdot \mathbf{B}^{\nabla}_{Iy}(\mathbf{x}_L) + (z - z_L) \cdot \mathbf{B}^{\nabla}_{Iz}(\mathbf{x}_L) \quad (44)$$

where $\widehat{\mathbf{B}}_I$ is the expanded shape function gradient matrix, $\widetilde{\mathbf{B}}_I$ is the smoothed shape function gradient matrix from SCNI or SNNI following (43), and $\mathbf{B}^{\nabla}_{Ix}$, $\mathbf{B}^{\nabla}_{Iy}$, and $\mathbf{B}^{\nabla}_{Iz}$ are the smoothed gradients of the implicit gradients in the x-, y-, and z-directions, respectively. Therefore, the stiffness matrix becomes:

$$\int_{\Omega} \widehat{\mathbf{B}}_I^T \mathbb{C} \widehat{\mathbf{B}}_J d\Omega = \sum_{L=1}^{NP} \left(\widetilde{\mathbf{B}}_I^T \mathbb{C} \widetilde{\mathbf{B}}_J V_L + \mathbf{B}_{Ix}^{\nabla T} \mathbb{C} \mathbf{B}_{Jx}^{\nabla} M_{Lx} + \mathbf{B}_{Iy}^{\nabla T} \mathbb{C} \mathbf{B}_{Jy}^{\nabla} M_{Ly} + \mathbf{B}_{Iz}^{\nabla T} \mathbb{C} \mathbf{B}_{Jz}^{\nabla} M_{Lz} \right) \tag{45}$$

where M_{Lx}, M_{Ly}, and M_{Lz} are the second moments of inertia about node L, and we have assumed that the contributions of the first moments of inertia and products of inertia are nullity if the nodes are at the centroids of the nodal representative domains.

In our numerical examples, SCNI and SNNI with NSNI stabilization are used to calculate gradient terms in Lagrangian and semi-Lagrangian regions, respectively. All other terms in the integrals of Eqs. (17) and (18) are evaluated at the node. The pressure projection term given by Eq. (19) may be calculated by evaluating the shape functions at the centroids of the sub-cells which, in two dimensions, is given as [59, 67]:

$$\Pi(\Psi_I)\Big|_{\Omega_L} = \frac{1}{A_L} \int_{\Omega_L} \Psi_I d\Omega \approx \frac{1}{A_L} \sum_{C=1}^{NSC} \Psi_I \left(\mathbf{x}_L^{S_C} \right) A_L^{S_C} \tag{46}$$

where $A_L = \sum_{C=1}^{NSC} A_L^{S_C}$ is the total nodal cell area (or volume) for node L, NSC is the total number of sub-cells of node L, $A_L^{S_C}$ is the Cth sub-cell area (or volume) of node L, and $\mathbf{x}_L^{S_C}$ is the centroid of the Cth sub-cell of node L. Hence, the pressure projection term may be evaluated as:

$$\begin{aligned} &\int_{\Omega_x} \varepsilon_f (\Psi_I - \Pi\Psi_I) \left(p^h - \Pi p^h \right) d\Omega \\ &= \sum_{L=1}^{NP} \left\{ \varepsilon_f(\mathbf{x}_L) \left[\Psi_I(\mathbf{x}_L) - \frac{1}{A_L} \sum_{C=1}^{NSC} \Psi_I \left(\mathbf{x}_L^{S_C} \right) A_L^{S_C} \right] \right. \\ &\quad \left. \left[p^h(\mathbf{x}_L) - \frac{1}{A_L} \sum_{C=1}^{NSC} p^h \left(\mathbf{x}_L^{S_C} \right) A_L^{S_C} \right] A_L \right\} \end{aligned} \tag{47}$$

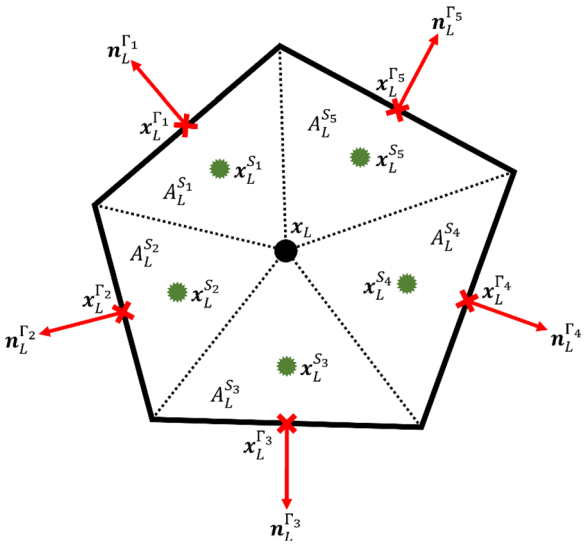

Fig. 5 Example of a conforming nodal cell centered on node L and located at $\mathbf{x}_L$; shape functions for calculating smoothed gradients are evaluated at the center of each nodal boundary segment, $\mathbf{x}_L^{\Gamma_i}$, which have outward normals $\mathbf{n}_L^{\Gamma_i}$; shape functions for calculating the pressure projection are evaluated at the centroids of the sub-cells, $\mathbf{x}_L^{S_i}$; the sub-cell areas are denoted by $A_L^{S_i}$

See Fig. 5 for an example of a conforming cell and evaluation points [67].

Matrix form and time integration

By substituting the RKPM approximations of Eqs. (13) through (16) into Eqs. (17) and (18), we arrive at the following matrix equations [59, 67]:

$$\mathbf{M}^{u}_{n+1}\ddot{\mathbf{U}}_{n+1} = \mathbf{F}^{u,\text{ext}}_{n+1} - \mathbf{F}^{u,\text{int}}_{n+1} \tag{48}$$

$$\mathbf{M}^{p}_{n+1}\dot{\mathbf{P}}_{n+1} = \mathbf{F}^{p,\text{ext}}_{n+1} - \mathbf{F}^{p,\text{int}}_{n+1} \tag{49}$$

where:

$$\mathbf{M}^{u}_{IJ} = \int_{\Omega_x} \Psi_I \rho \Psi_J d\Omega \mathbf{I} \tag{50}$$

$$\mathbf{F}^{u,\text{ext}}_{I} = \int_{\Omega_x} \Psi_I \rho \mathbf{g} d\Omega + \int_{\Gamma^t_x} \Psi_I \bar{\mathbf{t}} d\Gamma \tag{51}$$

$$\mathbf{F}^{u,int}_{I} = \int_{\Omega_x} \mathbf{B}^{u\,T}_{I} \cdot \widetilde{\boldsymbol{\sigma}}\left(\mathbf{u}^h\right) d\Omega - \int_{\Omega_x} \mathbf{B}^{u\,T}_{I} \cdot \left(\alpha S^w p^h \mathbf{1}\right) d\Omega \tag{52}$$

$$M^{p}_{IJ} = \int_{\Omega_x} \Psi_I Q^{-1} \Psi_J d\Omega \tag{53}$$

$$F^{p,\text{ext}}_{I} = \int_{\Omega_x} \mathbf{B}^{p\,T}_{I} \cdot \mathbf{k}^w \cdot S^w \rho^w \mathbf{g} d\Omega + \int_{\Gamma^q_x} \Psi_I \mathbf{n}_{\text{q}} \cdot \overline{\mathbf{q}} d\Gamma \tag{54}$$

$$F^{p,int}_{I} = \int_{\Omega_x} \Psi_I \alpha \nabla_{\mathbf{x}} \cdot \dot{\mathbf{u}}^h d\Omega + \int_{\Omega_x} \mathbf{B}^{p\,T}_{I} \cdot \mathbf{k}^w \cdot \nabla_{\mathbf{x}} p^h d\Omega + \int_{\Omega_x} \varepsilon_f (\Psi_I - \Pi\Psi_I)\left(p^h - \Pi p^h\right) d\Omega \tag{55}$$

and $\widetilde{\boldsymbol{\sigma}}$ is the effective stress tensor in Voigt notation, $\mathbf{B}^u_I$ and $\mathbf{B}^p_I$ are the shape function gradient matrices for the displacement and pressure fields, respectively, $\mathbf{I}$ is the second-order identity tensor, and $\mathbf{1}$ is the second-order identity tensor in Voigt notation.

For all numerical examples, Newmark's explicit, central difference scheme is used to discretize the solid equation in time, and the explicit, forward Euler scheme is used for the water pressure equation. A staggered approach is taken to couple the solid linear momentum and the pore water continuity equations. For the initial step, the solid momentum equation is solved for the displacements which are then used in the continuity equation to solve for the pressures. The newest displacements and pressures are used in the solid momentum equation for the next time step, and the cycle repeats.

Coupled Lagrangian/semi-Lagrangian reproducing kernel particle method

The recalculation of the RK shape functions at every time step in the semi-Lagrangian approach comes with a high computational cost. Following the formulation in [62], we combine the L-RK and the SL-RK formulations such that the SL-RK formulation is used

only in those regions of the domain where severe deformations occur to the extent that the deformation gradient is ill-conditioned or its inverse is not unique, and a L-RK formulation is used everywhere else. Like the FEM/meshfree coupling found in [63], this coupling is accomplished using a transition zone where L-RK and SL-RK shape functions and their derivatives are blended through a ramp function thus guaranteeing consistency in the approximation. The blending is given as:

$$u_i^h(\mathbf{x},t) = \sum_{I=1}^{NP} \Big[(1 - r(\mathbf{x},t)) \Psi_I^L(\mathbf{X}(\mathbf{x},t)) + r(\mathbf{x},t) \Psi_I^{SL}(\mathbf{x}) \Big] d_{Ii}(t) \tag{56}$$

where $r(\mathbf{x},t)$ is the ramp function and $d_{Ii}(t)$ is the ith component of the generalized displacement associated with node I. In [62], the ramp function is a predefined function in space and does not evolve in time:

$$r(\mathbf{x}) = \begin{cases} 0 & \text{for } w_{tr} \leq D(\mathbf{x}) \\ 1 - \frac{D(\mathbf{x})}{w_{tr}} & \text{for } 0 < D(\mathbf{x}) < w_{tr} \\ 1 & \text{for } D(\mathbf{x}) \leq 0 \end{cases} \tag{57}$$

where w_{tr} is the width of the transition region and $D(\mathbf{x})$ is the distance function measuring the distance from the predefined SL-RK region's boundary Γ_{SL} as a function of $\mathbf{x}$. The distance function is given by:

$$D(\mathbf{x}) = (\mathbf{x}_{SL} - \mathbf{x}) \cdot \mathbf{n} \tag{58}$$

where $\mathbf{x}_{SL}$ is the closest point to $\mathbf{x}$ on Γ_{SL} and $\mathbf{n}$ is the outward unit normal on Γ_{SL} at $\mathbf{x}_{SL}$. We denote this type of ramp function as Type-1 ramp function. The Type-1 ramp function uses Lagrangian ($r = 0$), transition ($0 < r < 1$), and semi-Lagrangian ($r = 1$) regions that are predefined and fixed for the entire simulation.

However, the regions that undergo extreme deformation are not known a priori in many practical applications, which makes the Type-1 ramp function ineffective. The Type-1 ramp function can be extended by allowing the SL-RK region to evolve based on a certain criterion, e.g., a criterion based on the deformation gradient or plastic strain. In this case, the SL-RK region is based on point clouds, and the boundary of the pointwise SL-RK region can be determined by techniques such as level set algorithms similar to that used for the kernel contact algorithms in Section 3.3 of [49]. If the SL boundary is determined by a level set function, the surface normal $\boldsymbol{n}$ can be easily determined by taking the gradient of the level set function. However, it may be time-consuming to detect the evolving boundaries of multiple SL-RK regions to define the associated transition

Table 1 The difference between internal forces generated by two RK shape functions with different support sizes in a one-dimensional stressed rod, where a denotes the RK normalized support size

Stress	Internal forces		Difference (%)
	$a = 3.0$	$a = 1.5$	
x	−0.16039	−0.16252	1
x^2	−0.00452	0.00599	176
x^3	−0.01140	−0.00442	158
x^4	−0.00111	0.00031	453

regions based on the minimum distance described in (57)–(58). To bypass such complexity, in our study, we propose a deformation-driven ramp function (Type-2 ramp function) that is a function of equivalent plastic strain (EPS) $\overline{\varepsilon}(\mathbf{x}, t)$:

$$r(\overline{\varepsilon}(\mathbf{x}, t)) = \begin{cases} 0 & \text{for } \overline{\varepsilon} \leq \overline{\varepsilon}_1 \\ 1 - \frac{\overline{\varepsilon}(\mathbf{x},t) - \overline{\varepsilon}_1}{\overline{\varepsilon}_2 - \overline{\varepsilon}_1} & \text{for } \overline{\varepsilon}_1 < \overline{\varepsilon} \leq \overline{\varepsilon}_2 \\ 1 & \text{for } \overline{\varepsilon} > \overline{\varepsilon}_2 \end{cases} \tag{59}$$

where $\overline{\varepsilon}_1$ and $\overline{\varepsilon}_2$ are the lower and upper EPS limits of the transition zone. As EPS is a function of both space and time, the deformation-driven ramp function evolves in response to the state of deformation. The ramp function defined in (59) automatically determines the semi-Lagrangian zone ($r = 1$) for the region where the deformation is large ($\overline{\varepsilon} \geq \overline{\varepsilon}_2$). Note that EPS is computed pointwise, and so, the ramp function is also computed pointwise. The ramp function for arbitrary $\mathbf{x}$ can be determined by RK interpolation of nodal values of the ramping function.

Since the transition from a L-RK shape function to a SL-RK shape function is gradual in time as well as in space during $\overline{\varepsilon}_1 < \overline{\varepsilon}(\mathbf{x}, t) \leq \overline{\varepsilon}_2$, a sudden jump in the internal force vector (55) from one time step to the next is prevented and thus a spurious wave generation can be avoided. Table 1 shows that the difference between internal forces $\mathbf{F}_I^{int} = \int_{\Omega_x} \widetilde{\mathbf{B}}_I \cdot \boldsymbol{\sigma} d\Omega$ (with $\widetilde{\mathbf{B}}_I$ the smoothed RK shape function gradient matrix and $\boldsymbol{\sigma}$ the Cauchy stress tensor) calculated by two RK shape functions with different support sizes in a one-dimensional stressed rod can be quite significant. Since a row-sum lumped mass matrix is used in this paper, the nodal mass will not change with the change in support size of RK shape functions satisfying the partition of unity. This indicates that a sudden change in internal force caused by, for example, an instant switch from L-RK to SL-RK approximations can produce nonphysical accelerations and, thus, wave propagation. A gradual transition of RK shape functions suppresses unphysical wave propagation that occurs when the transition is sudden, which is discussed later in "Poroelastic wave propagation" section.

If one were to differentiate Eq. (56) to get the shape function gradients, one would have to take the derivative of the ramp function which would lead to discontinuities across the transition zone's interface. To avoid this, we simply apply the same blending procedure to the shape function gradients as we did to the shape functions in Eq. (56):

$$\begin{aligned} \frac{\partial u_i^h(\mathbf{x}, t)}{\partial x_j} &= \sum_{I=1}^{NP} \left[(1 - r(\mathbf{x}, t)) \frac{\partial \Psi_I^L(\mathbf{X})}{\partial x_j} + r(\mathbf{x}, t) \frac{\partial \Psi_I^{SL}(\mathbf{x})}{\partial x_j} \right] d_{Ii}(t) \\ &= \sum_{I=1}^{NP} \left[(1 - r(\mathbf{x}, t)) \frac{\partial \Psi_I^L(\mathbf{X})}{\partial X_k} F_{kj}^{-1} + r(\mathbf{x}, t) \frac{\partial \Psi_I^{SL}(\mathbf{x})}{\partial x_j} \right] d_{Ii}(t) \end{aligned} \tag{60}$$

where $\mathbf{F}^{-1}$ is calculated by computing $\mathbf{F}$ using L-RK and then taking the direct inversion of $\mathbf{F}$. This necessitates $\mathbf{F}$ be invertible in the L–SL transition region. The time derivatives of the L-RK and SL-RK approximations can be blended in the same way:

$$\dot{u}_i^h(\mathbf{x},t) = \sum_{I=1}^{NP} \left[\left[(1 - r(\mathbf{x},t))\Psi_I^L(\mathbf{X}) + r(\mathbf{x},t)\Psi_I^{SL}(\mathbf{x}) \right] \dot{d}_{Ii}(t) + r(\mathbf{x},t)\Psi_I^*(\mathbf{x}) d_{Ii}(t) \right] \tag{61}$$

where, just as the spatial derivative of the ramp function is ignored in Eq. (60), so the time derivative of the ramp function is also ignored in Eq. (61). The term $\Psi_I^*(\mathbf{x})$ is due to the time derivative of the SL-RK shape function $\Psi_I^{SL}(\mathbf{x})$; see [53, 57].

A one-dimensional von Neumann stability analysis of the spatiotemporal Lagrangian/semi-Lagrangian coupling was performed in [62] based on a row-sum lumped mass matrix, a uniform nodal spacing of ΔX in the undeformed configuration, a uniform deformation with a one-dimensional deformation gradient F, and a central difference time integration scheme. The critical time step for the solid equation was found to be:

$$\Delta t_{cr}^u = \beta \sqrt{\frac{m^u \Delta x}{E\overline{A}}} \tag{62}$$

where m^u is the nodal lumped mass, E is the Young's modulus, β is a parameter measuring the ratio of non-conforming (SNNI) nodal cell length to conforming (SCNI) nodal cell length, $\Delta x = \Delta X \cdot F$, and $\overline{A}$ is given as:

$$\overline{A} = \left[(1 - r)A^L + rA^{SL} \right]^2 \tag{63}$$

where r is the ramp function which, to simplify the analysis, is assumed to be constant, and the definitions of A^L and A^{SL} are given in Appendix. Along with the property of $\overline{A}$ in (63), we choose [62]:

$$\Delta t_{\mathrm{cr}}^u = \min\left(\Delta t_{cr}^{u,L} = \frac{\beta}{A^L}\sqrt{\frac{m^u \Delta x}{E}}, \Delta t_{cr}^{u,SL} = \frac{\beta}{A^{SL}}\sqrt{\frac{m^u \Delta x}{E}} \right) \tag{64}$$

Thus, selecting a time step for which both pure L-RK and pure SL-RK simulations would be stable will guarantee the stability of the coupled L–SL RK simulation [62].

For the pore-water conservation of mass Eq. (18), we follow a similar procedure. Since we are using a staggered approach to the coupling, we ignore the term containing the solid velocity. In 1D, this leaves us with:

$$\mathbf{M}^p \dot{\mathbf{P}} = -\mathbf{F}^{p,\mathrm{int}} \tag{65}$$

where:

$$M_{IJ}^p = \int_{\Omega_x} \Psi_I Q^{-1} \Psi_J d\Omega \tag{66}$$

$$F_I^{p,int} = \int_{\Omega_x} \hat{B}_I^{p^T} k^w \nabla_x p^h d\Omega \tag{67}$$

To yield the most restrictive time step and simplify our calculation, we assume that $S^w = 1$ over the entire domain and for all time. Given this, it follows from Eqs. (6), (10),

(11), and the equation for the permeability, $k^w = \left(k^{rw}/\mu^w\right)k^w_{in}$, that Q^{-1} and k^w are constant. After discretizing the time derivative using the forward Euler time integration scheme with a lumped mass and following the same procedure in [62], we obtain the following estimate for the critical time step:

$$\Delta t^p_{cr} = \frac{\beta^2 \Delta x m^p}{2k^w \overline{A}} \tag{68}$$

where $m^p = \int_{\Omega_x} \Psi_I(x) Q^{-1} d\Omega$ is the nodal lumped mass and β, Δx, and $\overline{A}$ are the same as in the solid time step analysis. As with the solid equation, we can be conservative and choose the time step to be less than both the separate L-RK and SL-RK critical time step estimates:

$$\Delta t^p_{\mathrm{cr}} = \min\left(\Delta t^{p,L}_{cr} = \frac{\beta^2 \Delta x m^p}{2k^w A^{L^2}}, \Delta t^{p,SL}_{cr} = \frac{\beta^2 \Delta x m^p}{2k^w A^{SL^2}}\right) \tag{69}$$

Thus, to satisfy both the solid equilibrium and pore-water continuity equations' time step restrictions, the critical time step for the staggered coupling should be chosen as:

$$\Delta t_{cr} = \min\left(\Delta t^p_{cr}, \Delta t^u_{cr}\right) \tag{70}$$

Numerical examples

In this section, the proposed coupled L–SL hydro-mechanical formulation is demonstrated through a series of numerical examples. For all the cases, the linear RK basis and the cubic B-spline kernel function with box-type kernel supports are used, and explicit time integration with lumped mass is employed.

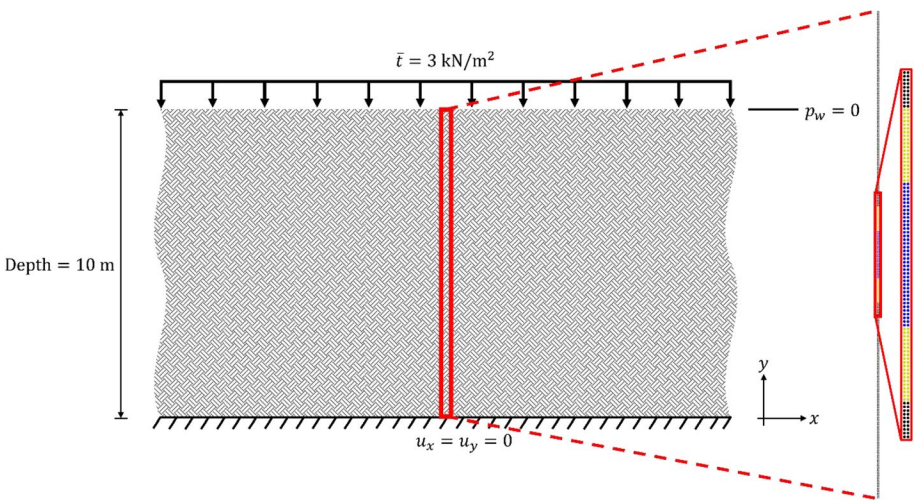

Fig. 6 Poroelastic wave propagation in soil with infinite dimension in x-direction and is discretized by coupled Lagrangian/semi-Lagrangian RK points in the y-direction; Lagrangian (black nodes), semi-Lagrangian (blue nodes), and transition (yellow nodes) regions for coupled L–SL formulation

Poroelastic wave propagation

The following example tests the robustness of both the pure semi-Lagrangian (SL) and the coupled Lagrangian/semi-Lagrangian (L–SL) formulations under elastodynamic conditions. As shown in Fig. 6, a layer of water saturated soil with infinite dimension in the x-direction and with a depth of 10 m in the y-direction is subjected to a uniform traction of $\bar{t} = 3\ \text{kN/m}^2$ at time $t = 0$. The top of the soil possesses a drained boundary condition, $p_w = 0$, and the bottom of the soil layer is assigned a fixed Dirichlet boundary condition, $u_x = u_y = 0$. A vertical layer of soil is discretized by Lagrangian, semi-Lagrangian, and L–SL coupling nodes. The soil properties follow [86]: Young's modulus $E = 254.42$ MPa, Poisson's ratio $\nu = 0.298$, solid grain mass density $\rho_s = 2700\ \text{kg/m}^3$, water mass density $\rho_w = 1000\ \text{kg/m}^3$, porosity $n^f = 0.48$, permeability $k^w = 3.55 \times 10^{-9}\ \text{m}^2/\text{Pa·s}$, bulk modulus of the solid grains $K^s = 1.1 \times 10^{10}$ Pa, bulk modulus of water $K^w = 3.3 \times 10^9$ Pa.

Two cases were run. The first case is the coupled L–SL formulation with a static coupling zone. Figure 6 shows the Lagrangian (322 black nodes), semi-Lagrangian (39 blue nodes), and transition (40 yellow nodes) regions in the vertical direction for the entire simulation. The horizontal direction is discretized by only two nodes with a plane-strain assumption.

The second case is the pure SL formulation. Both cases were compared with a pure Lagrangian case with 2001 nodes in the vertical direction, which serves as the reference solution for the pure SL and coupled L–SL cases. To examine the robustness of both coupled L–SL and pure SL cases, we intentionally varied the support sizes of the semi-Lagrangian nodes cyclically as follows:

$$a(t) = a_0\left[1 + 0.25\sin\left(\frac{2\pi t}{T}\right)\right] \tag{71}$$

where $a(t)$ is the support size, a_0 is the original support size, and T is the total time. This challenged the robustness of the SL-RK formulation to yield oscillations during support size change. The change in kernel shape over time is illustrated in Fig. 7.

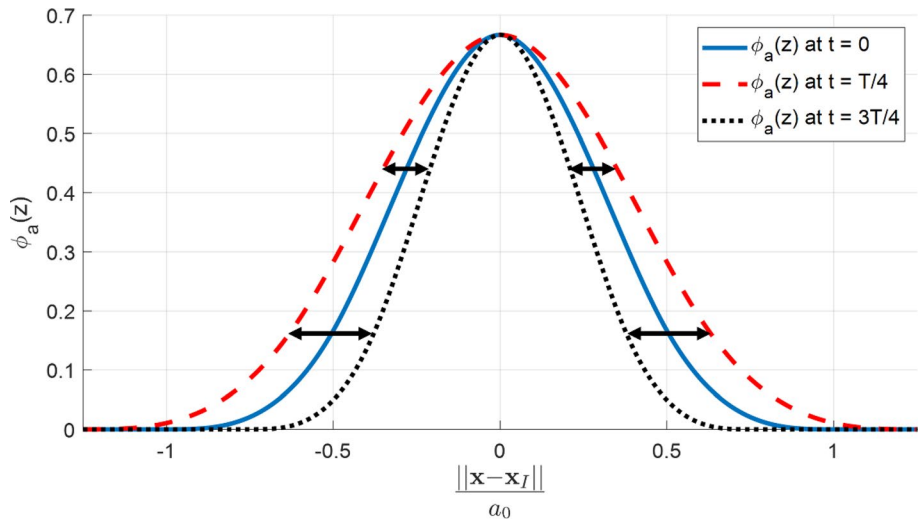

Fig. 7 Change in kernel shape over time

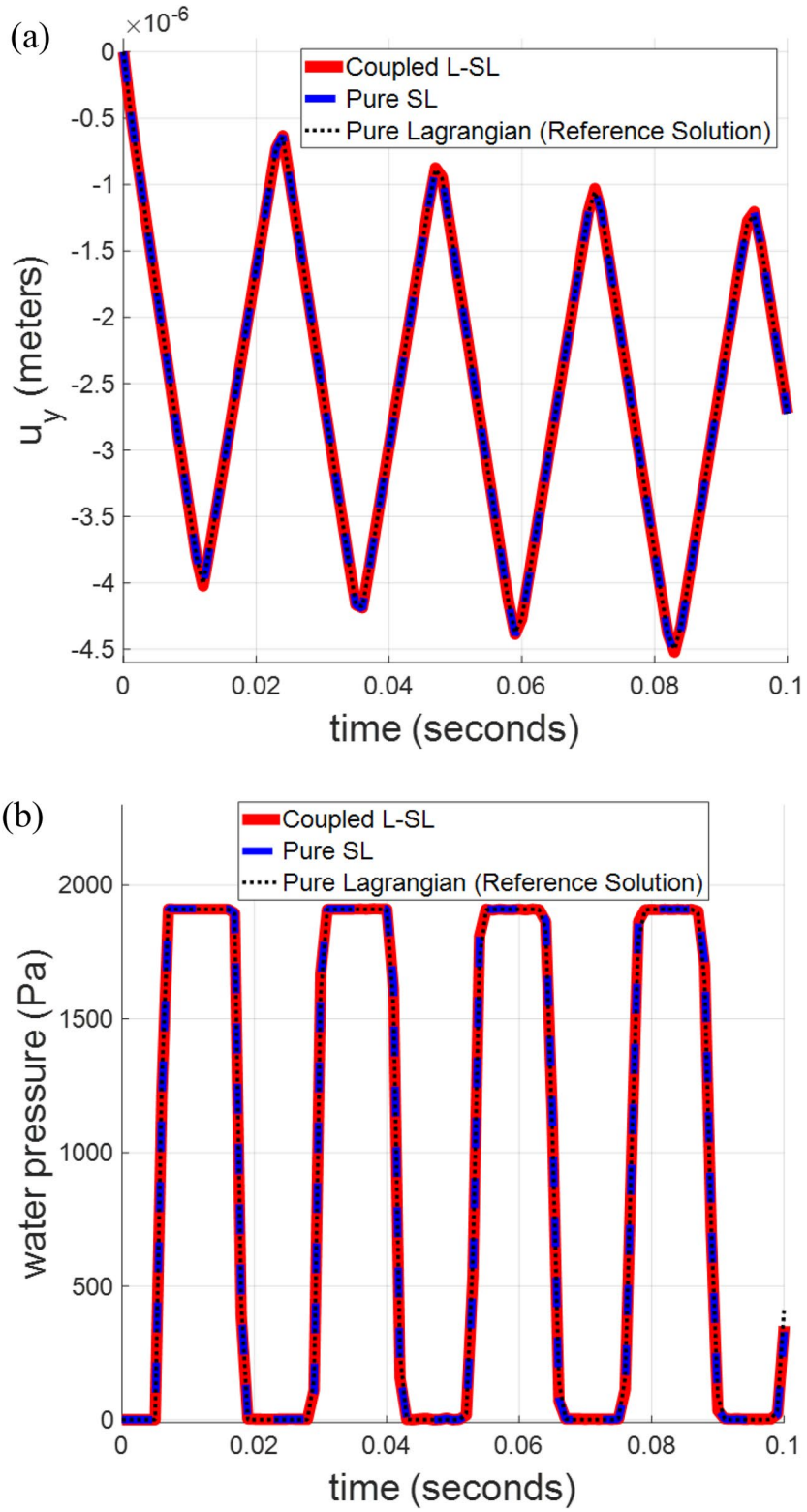

Fig. 8 Plot of solid grain displacement vs. time at the top of the soil layer (**a**); plot of water pressure vs. time at the bottom of the soil layer (**b**); both RKPM models used 401 nodes in the *y*-direction; the reference solution used was a pure L-RK formulation with 2001 nodes in the *y*-direction

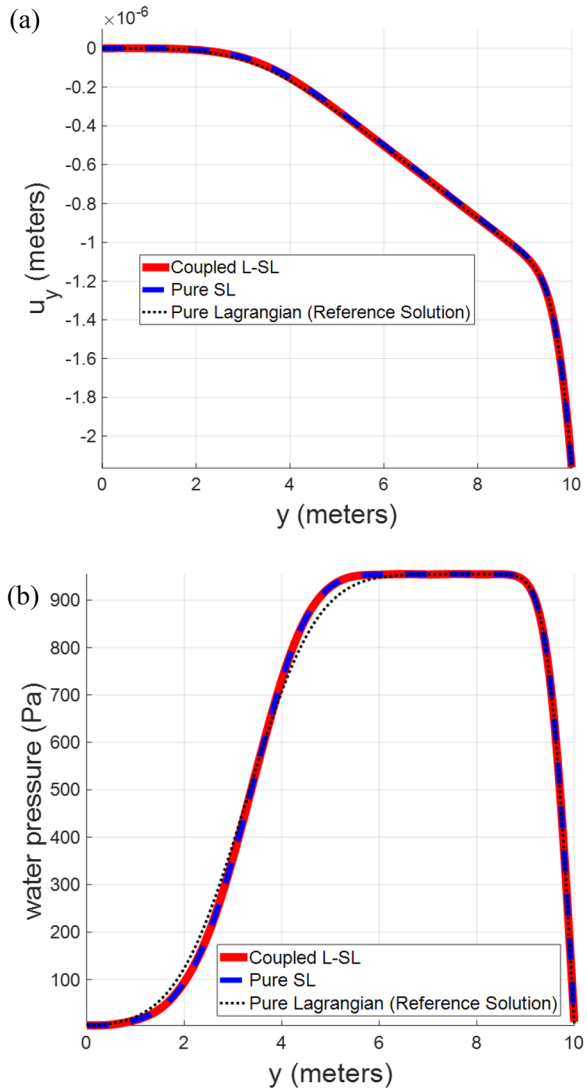

Fig. 9 Plot of y-displacement over the entire soil layer at $t = 0.075$ s (**a**); plot of water pressure over the entire soil layer at $t = 0.075$ s (**b**); both RKPM models used 401 nodes in the y-direction; the reference solution used was a pure L-RK formulation with 2001 nodes in the y-direction

Figure 8 displays the results for the y-displacement at the top of the soil layer (a) and the water pressure at the bottom of the soil layer (b). Both coupled L–SL and pure SL cases are found to closely match the reference L-RK solution.

Both coupled L–SL and pure SL simulations were run on a single CPU core (2.3 GHz). The L–SL simulation took 1730 s while the pure SL simulation took 5380 s, yielding an approximately 67.8% reduction in computational cost for the coupled L–SL RK formulation. Note that, for the coupled L–SL model, approximately 20% of the total RK nodes belong to either the SL zone or the transition zone, and therefore, only 20% of the shape functions were recomputed every time step.

Figure 9 displays the results for the y-displacement over the entire soil layer at $t = 0.075$ s (a) and the water pressure over the entire soil layer at $t = 0.075$ s (b). Again, both coupled L–SL RK and pure SL-RK cases are found to closely match the reference L-RK solution.

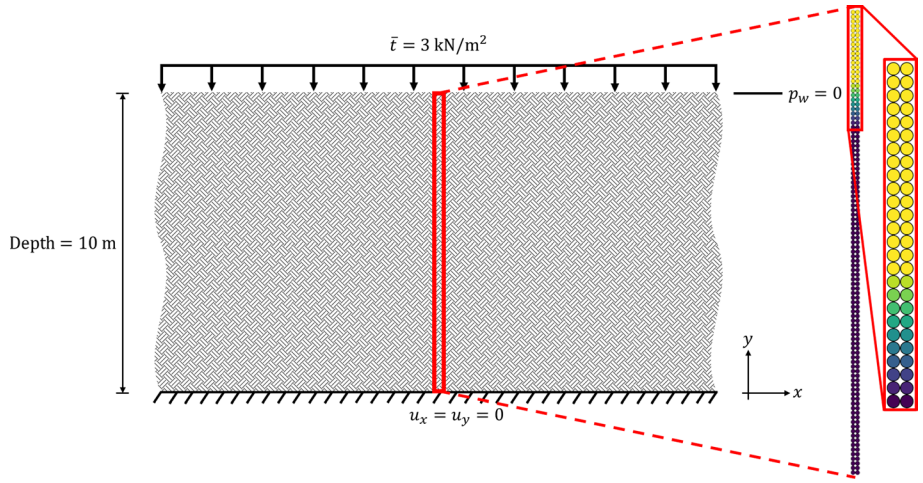

Fig. 10 Base ramping function $\bar{r}(y)$ for the two L–SL cases: the yellow and dark purple colors denote $\bar{r} = 1$ and $\bar{r} = 0$, respectively. $\bar{r}$ linearly changes in space

Table 2 Sudden and gradual temporal transitions from L-RK to SL-RK approximations in time and space; the y-coordinate is measured from the bottom of the soil layer

Depths	Sudden transition		Gradual transition		
	$0 \le t < 0.05$	$t \ge 0.05$	$0 \le t < 0.025$	$0.025 \le t < 0.05$	$t \ge 0.05$
8.5 m $< y \le$ 10 m	Lagrangian	semi-Lagrangian	Lagrangian	Transition in time	semi-Lagrangian
7.5 m $< y \le$ 8.5 m	Lagrangian	Transition in space	Lagrangian	Transition in space and time	Transition in space
0 m $< y \le$ 7.5 m	Lagrangian	Lagrangian	Lagrangian	Lagrangian	Lagrangian

Lastly, the effect of a gradual vs. a sudden transition from L-RK to SL-RK approximations in the time domain was investigated. The same domain was discretized with 101 RK nodes in the y-direction. Three cases were run with all three cases starting as pure Lagrangian discretizations. The first case stays pure L-RK throughout the simulation and serves as the reference solution. For the second and third cases, a temporal transition is made to a coupled Lagrangian/semi-Lagrangian discretization with the approximations over space and time. The ramping function $r(y,t)$ is defined as

$$r(y,t) = \alpha(t)\bar{r}(y), \tag{72}$$

with the base ramping function $\bar{r}(y)$ defined as

$$\bar{r}(y) = \begin{cases} 0, & y \le 7.5 \\ y - 7.5 & 7.5 < y \le 8.5 \\ 1, & 8.5 < y \le 10 \end{cases}, \tag{73}$$

as shown in Fig. 10. For the second case, the temporal transition happens suddenly at $t = 0.05$ s with the scaling coefficient $\alpha(t)$ in (72) is written as

$$\alpha(t) = \begin{cases} 0, & t < 0.05 \\ 1, & t \ge 0.05 \end{cases}. \tag{74}$$

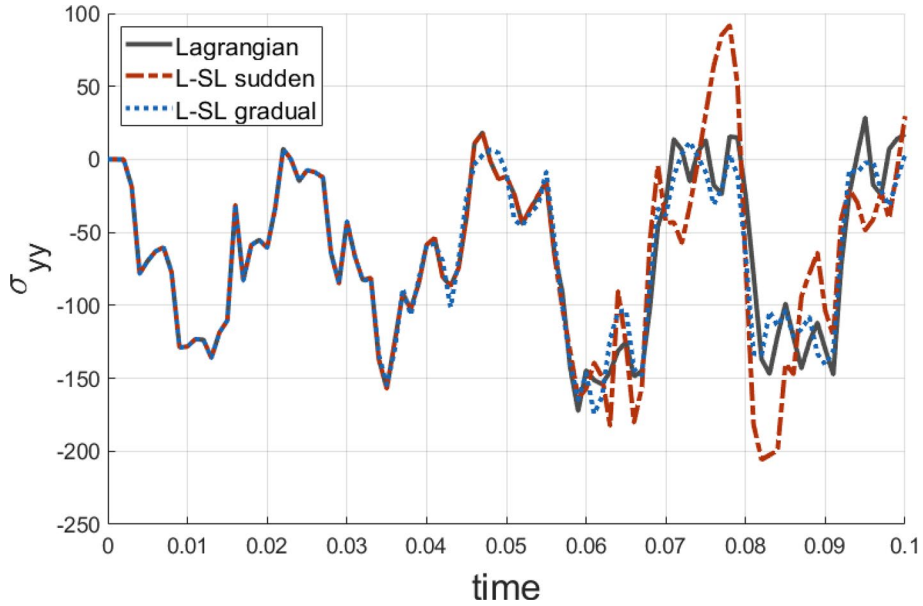

Fig. 11 Time history of the vertical stress at a depth of $y = 5.0$ m for pure L-RK, sudden transition L–SL RK, and gradual transition L–SL RK cases; the sudden transition occurs at $t = 0.05$ s; the gradual transition occurs over 0.025 s $< t <$ 0.05 s where the support sizes are linearly ramped over that period

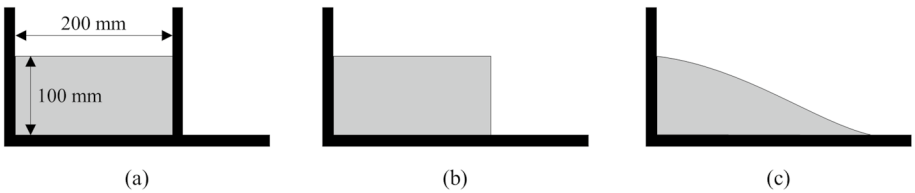

Fig. 12 Experimental procedure: **a** the granular column supported by two walls, **b** the soil column just after the right wall is removed, **c** collapsing granular column

In the third case, the temporal transition occurs gradually over 0.025 s $< t <$ 0.05 s where the supports are ramped linearly over that period, mimicking the gradual development of equivalent plastic strain:

$$\alpha(t) = \begin{cases} 0, & t < 0.025 \\ \frac{t-0.025}{0.025} & 0.025 \le t < 0.05 \\ 1, & t \ge 0.05 \end{cases}. \tag{75}$$

Note that the zone is fully semi-Lagrangian when $r(y,t) = 1$. The transition states for the two L–SL cases are summarized in Table 2. The normalized support sizes used for the L-RK and SL-RK shape functions are 3.0 and 1.05, respectively. A significantly smaller normalized support size is chosen for the SL-RK shape functions compared to the L-RK shape functions to mimic a highly stretched material to challenge the robustness of the proposed method. The time histories of the vertical stress, σ_{yy}, at $y = 5.0$ m for all three cases are shown in Fig. 11 where artificial oscillations are present in the second, sudden transition case while only a slight deviation from the pure Lagrangian

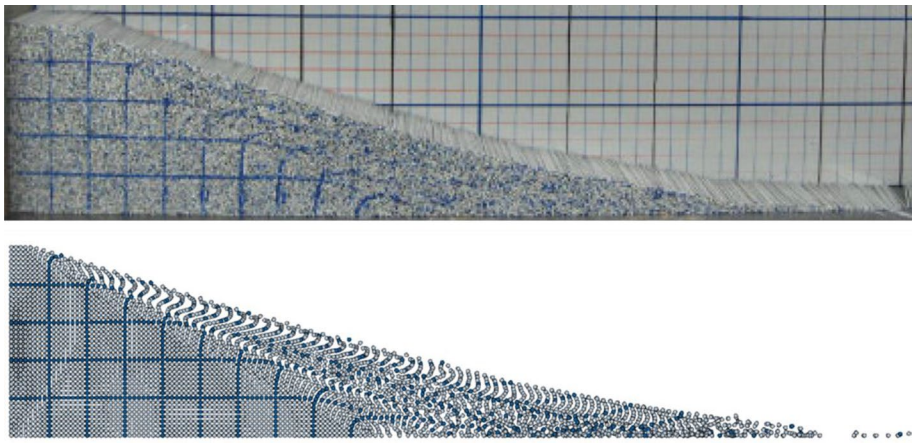

Fig. 13 Final configuration: (upper) experiment [87] and (lower) coupled L–SL RKPM simulation

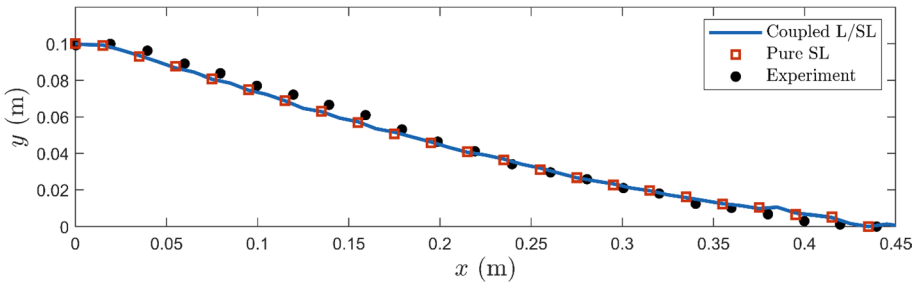

Fig. 14 Comparison of surface configurations obtained experimentally and numerically

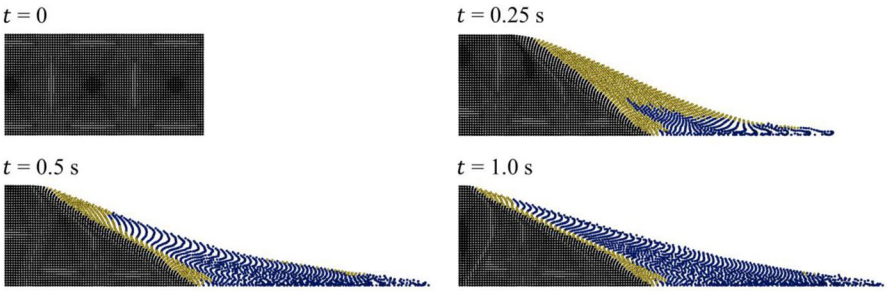

Fig. 15 Evolution of the semi-Lagrangian (blue nodes) and transition (yellow nodes) regions

reference solution is apparent in the third, gradual transition case. This illustrates the need for a smooth ramp function such as the one in Eq. (59).

Collapse of a granular column

To further demonstrate the capability of the proposed method to model landslide-type problems, the granular collapse experiment carried out by Bui et al. [87] is considered. In the experiment, aluminum granular material was packed in a 200 mm × 100 mm area supported by two walls. Then, the collapse was initiated by

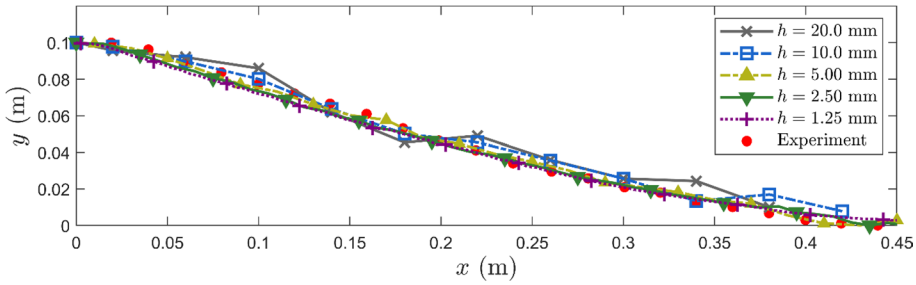

Fig. 16 Surface configurations for various levels of L–SL RK refinement: in the legend, *h* denotes the initial nodal spacing

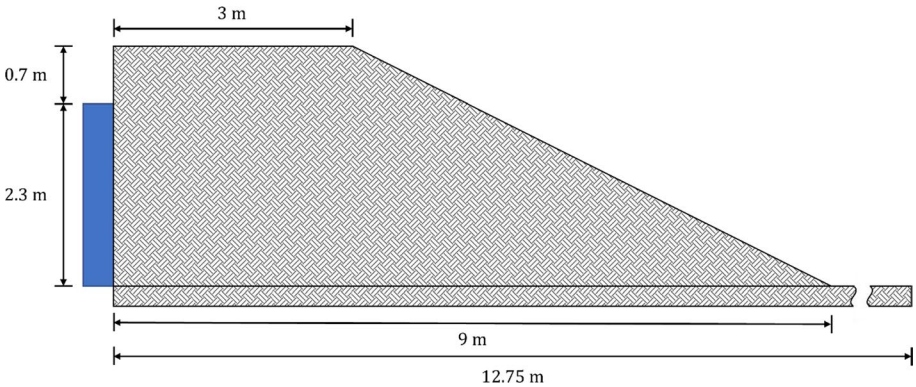

Fig. 17 Levee setup; blue shading on the left is the water table (modeled as a pressure boundary condition); the hatched pattern represents sandy soil

suddenly removing the right wall, as shown in Fig. 12. For the numerical simulations, the Drucker-Prager constitutive model is used with a cohesion of 0, a friction angle of 19.8°, a bulk modulus of 0.7 MPa, a Poisson's ratio of 0.3, and a mass density of 2,650 kg/m^3 [87]. For the evolution of the semi-Lagrangian zone, the Type-2 deformation-driven ramp function in Eq. (59) is used with $\overline{\varepsilon}_1 = 0.5$ and $\overline{\varepsilon}_2 = 2.0$. As the problem does not involve pore water, only the mechanical formulation is utilized for this numerical example. The domain is discretized by 6642 RK nodes (2 layers of 3321 RK nodes to model the plane strain problem in a 3-D code) with an initial nodal spacing of 2.5 mm and a normalized support size of 2.0.

Figures 13 and 14 show the collapsed soil and the surface configurations, respectively, obtained by the experiment and the L–SL RK simulations, and good agreement is observed. As shown in Fig. 15, nodes that were initially Lagrangian automatically evolve into semi-Lagrangian nodes when the deformation becomes large while the nodes in the non-collapsing region remain Lagrangian. The coupled L–SL simulation reduces the CPU time by approximately 35.5% compared to the pure SL simulation while also yielding a comparable result. Additionally, a numerical convergence study is performed for five different levels of domain refinement: 20 mm, 10 mm, 5 mm, 2.5 mm, and 1.25 mm. The final surface configurations predicted by the various discretizations are shown in Fig. 16, demonstrating solution convergence with refinement.

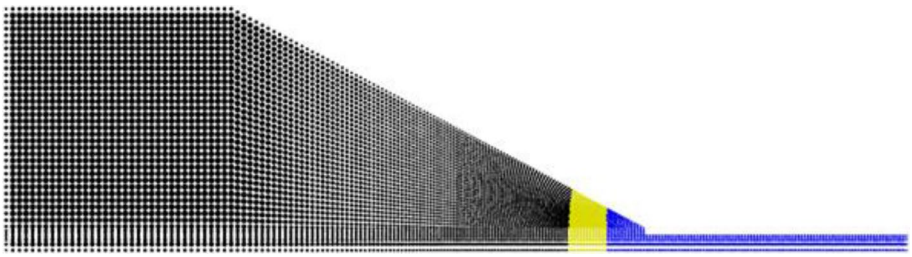

Fig. 18 Distribution of Lagrangian (black), semi-Lagrangian (blue), and transition region (yellow) nodes

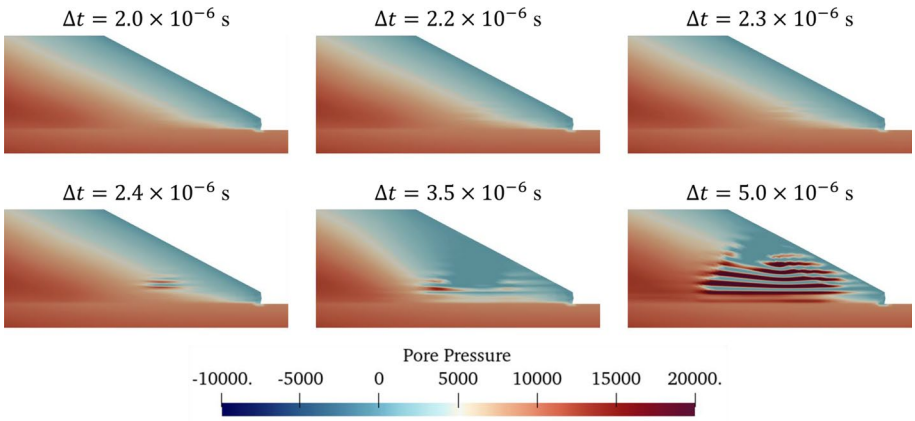

Fig. 19 Pore pressure distribution at $t = 0.04$ s

Seepage-induced levee failure

A seepage-induced slope failure of a sand levee based on the experiments described in [88–90] is simulated by the proposed L–SL RK. In this experiment, an initially unsaturated sand levee is subjected to a seepage flow generated by a constant water pressure on the levee's back surface as shown in Fig. 17. After about 13 h, the toe of the levee eventually develops material damage leading to the ultimate failure of the entire levee.

Given the scarcity of material data for the sandy soil used in the experiment, material properties from other works which modeled similar events were used [23, 24, 59, 91]: Young's modulus $E = 1.0 \times 10^7$ Pa, Poisson's ratio $\nu = 0.3$, gravitational acceleration $g = 9.806\,\mathrm{m/s^2}$, solid mass density $\rho^s = 2700\,\mathrm{kg/m^3}$, water mass density $\rho^w = 1000\,\mathrm{kg/m^3}$, porosity $n^f = 0.46$, intrinsic permeability $k_{in}^w = 5.1 \times 10^{-7}\,\mathrm{m^2}$, bulk modulus of the solid grains $K^s = 1.0 \times 10^{22}$ Pa, bulk modulus of water $K^w = 2.0 \times 10^9$ Pa. For the van Genuchten model for hydraulic conductivity, we used an irreducible water saturation $S^{rw} = 0.0842$ and empirical parameters $n = 2.0$, $m = 1 - 1/n$, and $\beta = 0.7\mathrm{m}^{-1}$. Finally, we utilized the Drucker-Prager plasticity model with a friction angle of 20° and a cohesion of 300 Pa.

Since the primary objective of this study was to model the post-failure runout, the time-dependent simulation began just as the levee was about to fail. The initial state of the effective stress and pore water pressure in the dynamic simulation was determined by a static simulation using the water level shown in Fig. 17, a method outlined in [69].

Figure 18 shows the RKPM discretization with Lagrangian (black), semi-Lagrangian (blue), and transition region (yellow) nodes for the L–SL RK coupled simulation. The

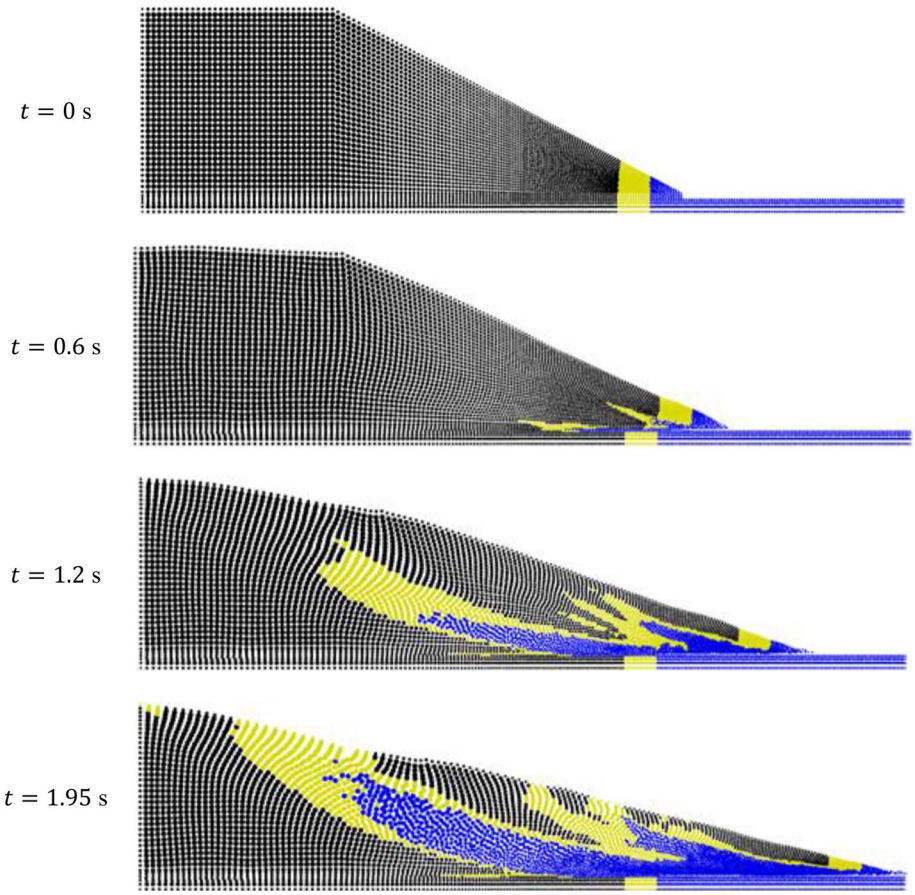

Fig. 20 Progressive levee failure for the coupled L–SL RK simulation plotting Lagrangian (black nodes), semi-Lagrangian (blue nodes), and transition (yellow nodes) regions

nodes at the toe of the levee were initialized as semi-Lagrangian since the deformation in that region becomes large soon after the simulation begins. For the evolution of the semi-Lagrangian zone, the Type-2 ramp function in Eq. (59) was used with $\overline{\varepsilon}_1 = 0.5$ and $\overline{\varepsilon}_2 = 1.0$. The normalized support size for both Lagrangian and semi-Lagrangian regions was 2.0.

We begin with testing various time steps for the early stage of the simulation to demonstrate the critical time step suggested in [70]. Considering the minimum nodal distance of 0.0158 m, the computed Δt^u_{cr} and Δt^p_{cr} are 4.41×10^{-4} s and 2.29×10^{-6} s, respectively. Therefore, $\Delta t_{cr} = \min\left(\Delta t^p_{cr}, \Delta t^u_{cr}\right) = 2.29 \times 10^{-6}$ s is obtained. Figure 19 shows the pore pressure distribution at $t = 0.04$ s. Although the instability is subtle for $\Delta t = 2.3 \times 10^{-6}$ s which barely exceeds the computed Δt_{cr} due to the non-uniform point distribution, the instability is clearly shown for the cases of $\Delta t \geq 2.4 \times 10^{-6}$ s. For the remaining section, $\Delta t = 2.0 \times 10^{-6}$ s is used.

Figure 20 shows the distribution of Lagrangian (black nodes), semi-Lagrangian (blue nodes), and transition (yellow nodes) regions during various stages of the levee's failure for the coupled L–SL simulation. Figure 21 compares the coupled L–SL and pure SL simulations at various stages of levee failure plotting equivalent plastic strain. Notice

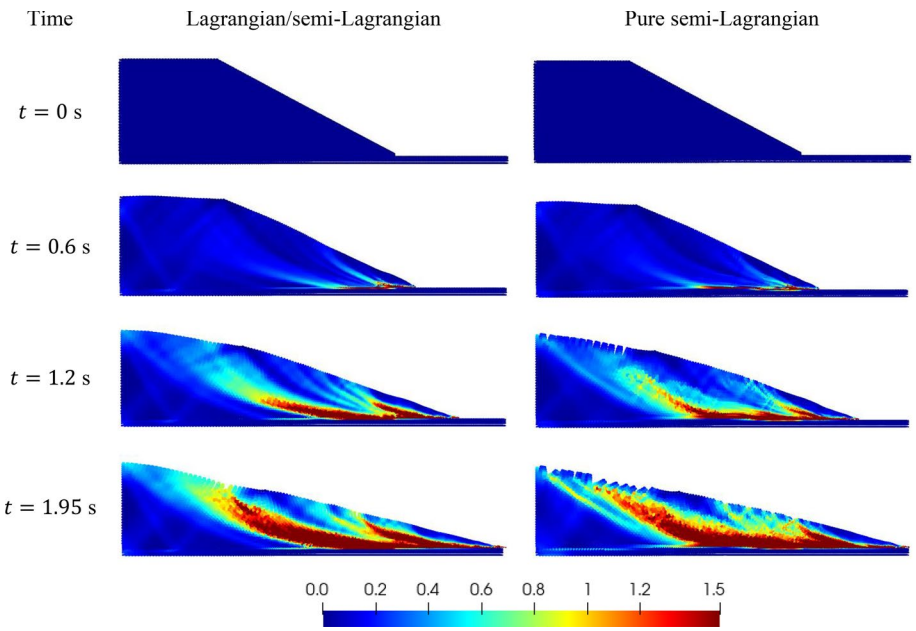

Fig. 21 Progressive levee failure plotting equivalent plastic strain: coupled Lagrangian/semi-Lagrangian (left) and pure semi-Lagrangian (right)

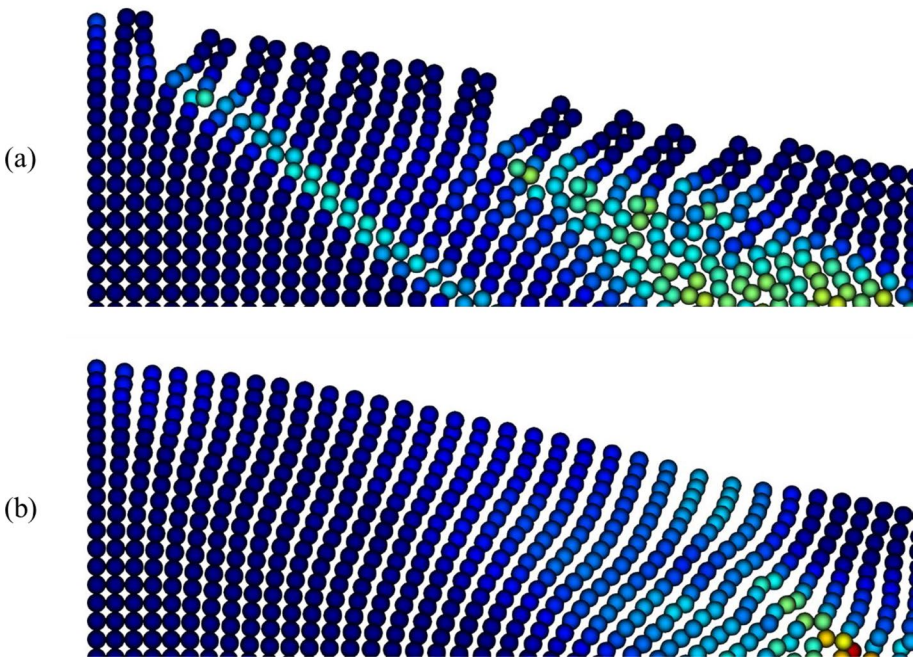

Fig. 22 Close-up of the top of the levee at $t = 1.5$ s for the pure SL-RK simulation (**a**) and coupled L–SL RK (**b**); numerical fracture occurs in the pure SL-RK case due to insufficient kernel support coverage of neighbors

the complex shear band formation in the latter stages of run-out. The coupled L–SL case yields a 37.5% CPU reduction compared to the pure SL case.

Figure 22 shows a close-up of the top of the levee at $t = 1.5$ s for both cases. The noticeable separation between clusters of nodes with node-to-node oscillation seen in

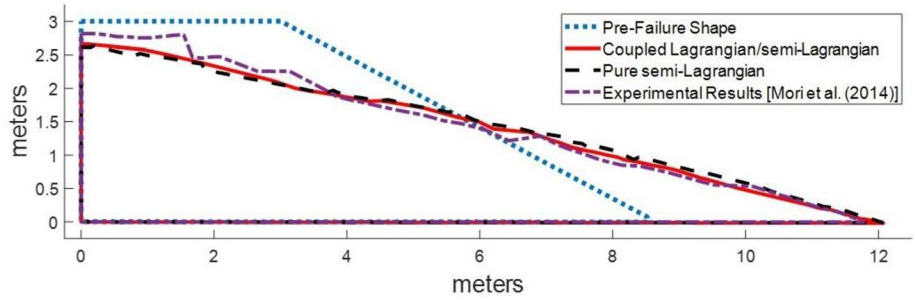

Fig. 23 Post-failure final shapes; the blue dotted line represents the pre-failure shape; the solid red line represents the coupled L–SL post-failure shape; the dashed black line represents the pure SL post-failure shape; the purple dot-dashed line represents the experimental results from [90]

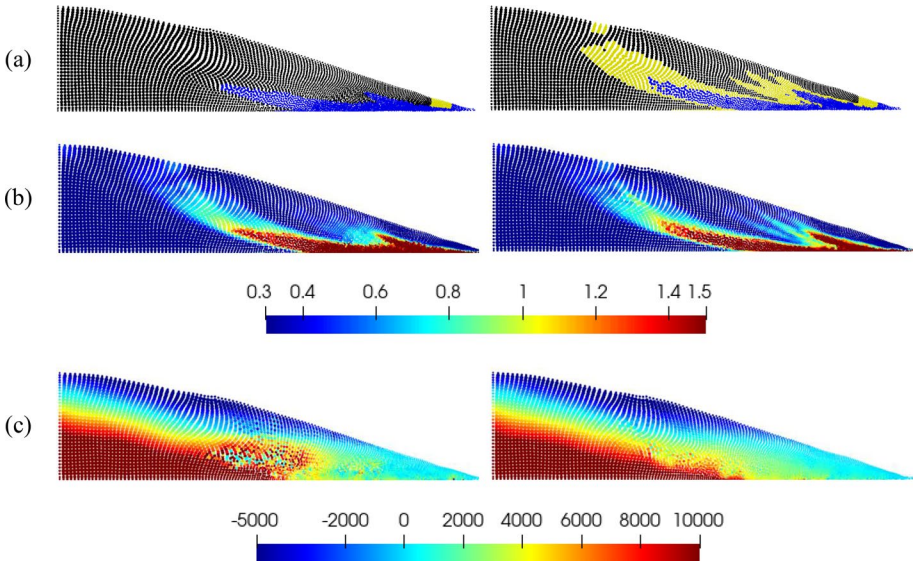

Fig. 24 Coupled L–SL simulation results $t = 1.35$ s obtained with sudden transition (left) and gradual transition (right): **a** L-RK (black), SL-RK (blue), and transition (yellow) zones; **b** equivalent plastic strain; **c** pore wave pressure field

the pure SL case is due to insufficient kernel support coverage of neighbors in the region where very high material stretch is presented, and as a result, numerical fracture occurs. This can be remedied by updating the support sizes with each time step, which is not activated for the purpose of comparison with the coupled L–SL RK approach. On the other hand, the coupled L–SL RK simulation without support update, suffers from this phenomenon to a lesser degree since the top of the levee is dominated by Lagrangian regions which precludes insufficient kernel coverage. In this manner, the coupled L–SL RK formulation provides better stability in the absence of time-consuming support updates. It is noteworthy to point out that the pure L-RK formulation is incapable of modeling the severe plastic flow and damage induced during the landslide process.

Finally, Fig. 23 compares the post-failure final shapes for the coupled L–SL (solid red line), pure SL (dashed black line), and the experimental results from Mori et al. [90]

(dot-dashed purple line) along with the pre-failure shape (dotted blue line). Both numerical cases clearly follow the experimental results quite well. Greater accuracy could potentially be achieved using a better constitutive model and material properties more closely aligned with the soil of the experiment.

Next, an additional coupled L–SL RK simulation is conducted to investigate the effect of Lagrangian to semi-Lagrangian transition in the time domain. In the previous case, the transition from Lagrangian to semi-Lagrangian is linearly ramped in time following Eq. (59). In this test case, the evolution from Lagrangian to semi-Lagrangian is made to occur suddenly, as shown in Fig. 24a, when the equivalent plastic strain becomes 1.0 without the presence of a transition zone both in space and time. As shown in Fig. 24b, c, the equivalent plastic strain field shows a less clear shear band formation, and the pore water pressure field presents a much more pronounced oscillation compared to the numerical results obtained by the L–SL simulation with a smooth transition.

Conclusion

In this work, we proposed a deformation-dependent coupling of the Lagrangian/semi-Lagrangian (L–SL) reproducing kernel approximation for computationally efficient and accurate hydro-mechanical simulation of landslides. While SL-RK, where the kernel functions are defined in the current configuration, has proven to be effective in extreme event modelling, the computational cost for the re-evaluation of the shape functions at every time step is a drawback. A selective employment of the SL-RK approximation can be a remedy, but the region where the SL-RK approximation is needed cannot be pre-determined in most cases. Therefore, an evolutionary blending of L-RK and SL-RK shape functions is introduced by employing a deformation-dependent evolving ramp function which depends on certain deformation measures, e.g., equivalent plastic strain which varies in space and time in this work. The gradual development of equivalent plastic strain yields a transition from Lagrangian to semi-Lagrangian states over time. This equivalent plastic strain-based deformation-dependent blending ensures spatial continuity and consistency in the spatial approximation and minimizes spurious oscillations in the solution which would happen if there was a sudden transition between states.

The proposed method was implemented in an equal-order mixed u–p RKPM formulation with a least-squares pressure projection stabilization. The critical time step of the proposed L–SL RKPM formulation was estimated and numerically verified. The capability of the proposed method was first demonstrated through a series of numerical examples including a poroelastic wave propagation problem under challenging kernel support conditions, a granular column collapse problem, and finally, a simulation of a seepage-induced levee failure leading to landslide. Comparison was made with a pure SL-RK simulation. The coupled L–SL RK simulation showed significant improvement over the pure SL-RK simulation both in terms of accuracy (e.g., less numerical fracture) as well as computational efficiency. Finally, it is noteworthy to point out that various forms of the deformation-driven blending function for the L–SL coupling are possible, and the proposed blending function based on equivalent plastic strain is just one natural choice for elastoplastic problems.

Appendix. Definitions of constants associated with critical time step

For stability analysis, a uniform discretization and a uniform deformation are considered as illustrated in Fig. 25. Then, the uniformity (76) and the symmetry (77) of the RK shape functions can be utilized as follows:

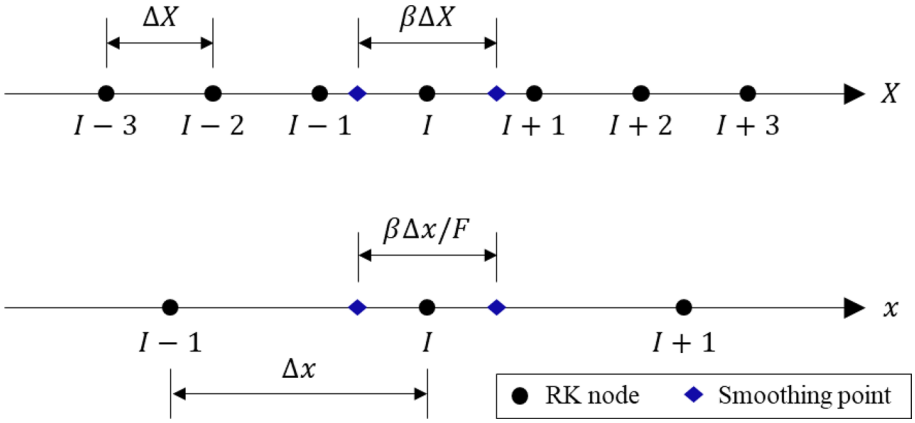

Fig. 25 Illustration of nodes and the smoothing point of node I in the reference and current configuration

$$\begin{aligned}\Psi_I^L(X_I + j\Delta X) &= \Psi_J^L(X_J + j\Delta X) \equiv \Psi^L(j\Delta X),\\ \Psi_I^{SL}(x_I + j\Delta x) &= \Psi_J^{SL}(x_J + j\Delta x) \equiv \Psi^{SL}(j\Delta x),\end{aligned} \tag{76}$$

$$\begin{aligned}\Psi^L(j\Delta X) &= \Psi^L(-j\Delta X),\\ \Psi^{SL}(j\Delta x) &= \Psi^{SL}(-j\Delta x),\end{aligned} \tag{77}$$

with $I, J, j \in \mathbb{Z}$. The constant A^{L} and A^{SL} in (63) are defined as follows:

$$\begin{aligned}A^L &= \sum_{j=1}^{(N^L-1)/2} \left[\psi^L(j\Delta X + \overline{C}) - \psi^L(j\Delta X - \overline{C})\right],\\ A^{SL} &= \sum_{j=1}^{(N^{SL}-1)/2} \left[\psi^{SL}(j\Delta x + \overline{c}) - \psi^{SL}(j\Delta x - \overline{c})\right],\end{aligned} \tag{78}$$

with $\overline{C} = 0.5\beta\Delta X$ and $\overline{c} = 0.5\beta\Delta x/F$ where β is defined in Fig. 25. In (78), N^L and N^{SL} denotes the number of neighbor nodes associated with the L-RK shape functions and the number of neighbor nodes associated with the SL-RK shape functions, respectively. Interested readers should consult [62] for details.

Acknowledgements

The support of this work by the Sandia National Laboratories to UC San Diego under Contract Agreement 1655264 is greatly acknowledged. Sandia National Laboratories is a multi-mission laboratory managed and operated by National Technology and Engineering Solutions of Sandia, LLC, a wholly owned subsidiary of Honeywell International Inc., for the U.S. Department of Energy's National Nuclear Security Administration under contract DE-NA0003525. This paper describes objective technical results and analysis. Any subjective views or opinions that might be expressed in the paper do not necessarily represent the views of the U.S. Department of Energy or the United States Government.

Author contributions

Equal contributions. All authors read and approved the final manuscript.

Funding
Sandia National Laboratories to UC San Diego under Contract Agreement 1655264.

Availability of data and materials
Not applicable.

Declarations

Competing interests
The authors declare that they have no competing interests.

Received: 18 May 2022 Accepted: 2 September 2022
Published online: 30 September 2022

References

1. Quecedo M, Pastor M, Herreros MI, Fernández Merodo JA. Numerical modelling of the propagation of fast landslides using the finite element method. Int J Numer Methods Eng. 2004;59(6):755–94.
2. Islam N, Hawlader B, Wang C, Soga K. Large-deformation finite-element modelling of earthquake-induced landslides considering strain-softening behaviour of sensitive clay. Can Geotech J. 2019;56(7):1003–18.
3. Chen X, Li D, Tang X, Liu Y. A three-dimensional large-deformation random finite-element study of landslide runout considering spatially varying soil. Landslides. 2021;18(9):3149–62.
4. Crosta GB, Imposimato S, Roddeman DG. Numerical modelling of large landslides stability and runout. Nat Hazard. 2003;3(6):523–38.
5. Crosta GB, Imposimato S, Roddeman D. Numerical modelling of entrainment/deposition in rock and debris-avalanches. Eng Geol. 2009;109(1–2):135–45.
6. Di Y, Yang J, Sato T. An operator-split ALE model for large deformation analysis of geomaterials. Int J Numer Anal Methods Geomech. 2007;31(12):1375–99.
7. Konuk I, Yu S, Evgin E. Application of the ALE FE method to debris flows. WIT Trans Ecol Environ. 2006;90:47–57.
8. Kwan JS, Koo RC, Ng CWW. Landslide mobility analysis for design of multiple debris-resisting barriers. Can Geotech J. 2015;52(9):1345–59.
9. Cheung AK, Yiu J, Lam HW, Sze EH. Advanced numerical analysis of landslide debris mobility and barrier interaction. HKIE Trans. 2018;25(2):76–89.
10. Luo HY, Zhang LL, Zhang LM. Progressive failure of buildings under landslide impact. Landslides. 2019;16(7):1327–40.
11. Liu WK, Chang H, Chen J-S, Belytschko T. Arbitrary Lagrangian–Eulerian Petrov–Galerkin finite elements for nonlinear continua. Comput Methods Appl Mech Eng. 1988;68(3):259–310.
12. Liu WK, Chen J-S, Belytschko T, Zhang YF. Adaptive ALE finite elements with particular reference to external work rate on frictional interface. Comput Methods Appl Mech Eng. 1991;93(2):189–216.
13. Cremonesi M, Ferri F, Perego U. A basal slip model for Lagrangian finite element simulations of 3D landslides. Int J Numer Anal Methods Geomech. 2017;41(1):30–53.
14. Jin Y-F, Yin Z-Y. Two-phase PFEM with stable nodal integration for large deformation hydromechanical coupled geotechnical problems. Comput Methods Appl Mech Eng. 2022;392: 114660.
15. Zhang X, Sheng D, Sloan SW, Bleyer J. Lagrangian modelling of large deformation induced by progressive failure of sensitive clays with elastoviscoplasticity. Int J Numer Methods Eng. 2017;112(8):963–89.
16. Jin Y, Yuan W, Yin Z, Cheng Y. An edge-based strain smoothing particle finite element method for large deformation problems in geotechnical engineering. Int J Numer Anal Methods Geomech. 2020;44(7):923–41.
17. Jin Y-F, Yin Z-Y, Yuan W-H. Simulating retrogressive slope failure using two different smoothed particle finite element methods: a comparative study. Eng Geol. 2020;279: 105870.
18. Jin Y-F, Yin Z-Y, Zhou X-W, Liu F-T. A stable node-based smoothed PFEM for solving geotechnical large deformation 2D problems. Comput Methods Appl Mech Eng. 2021;387: 114179.
19. Zhang X, Oñate E, Torres SAG, Bleyer J, Krabbenhoft K. A unified Lagrangian formulation for solid and fluid dynamics and its possibility for modelling submarine landslides and their consequences. Comput Methods Appl Mech Eng. 2019;343:314–38.
20. Salazar F, Irazábal J, Larese A, Oñate E. Numerical modelling of landslide-generated waves with the particle finite element method (PFEM) and a non-Newtonian flow model. Int J Numer Anal Methods Geomech. 2016;40(6):809–26.
21. Mulligan RP, Franci A, Celigueta MÁ, Take WA. Simulations of landslide wave generation and propagation using the particle finite element method. J Geophys Res Oceans. 2020. https://doi.org/10.1029/2019JC015873.
22. Zhang X, Krabbenhoft K, Sheng D, Li W. Numerical simulation of a flow-like landslide using the particle finite element method. Comput Mech. 2015;55(1):167–77.
23. Bandara S, Soga K. Coupling of soil deformation and pore fluid flow using material point method. Comput Geotech. 2015;63:199–214.
24. Soga K, Alonso E, Yerro A, Kumar K, Bandara S. Trends in large-deformation analysis of landslide mass movements with particular emphasis on the material point method. Géotechnique. 2016;66(3):248–73.
25. Liang Y, Zhang X, Liu Y. An efficient staggered grid material point method. Comput Methods Appl Mech Eng. 2019;352:85–109.
26. Wilson P, Wüchner R, Fernando D. Distillation of the material point method cell crossing error leading to a novel quadrature-based C0 remedy. Int J Numer Methods Eng. 2021;122(6):1513–37.
27. Bardenhagen SG, Kober EM. The generalized interpolation material point method. Comput Model Eng Sci. 2004;5(6):477–96.

28. Cleary PW, Prakash M. Discrete–element modelling and smoothed particle hydrodynamics: potential in the environmental sciences. Philos Trans R Soc Lond Ser A Math Phys Eng Sci. 2004;362(1822):2003–30.
29. Staron L. Mobility of long-runout rock flows: a discrete numerical investigation. Geophys J Int. 2008;172(1):455–63.
30. Wu J-H, Lin J-S, Chen C-S. Dynamic discrete analysis of an earthquake-induced large-scale landslide. Int J Rock Mech Min Sci. 2009;46(2):397–407.
31. Tang C-L, Hu J-C, Lin M-L, Angelier J, Lu C-Y, Chan Y-C, Chu H-T. The Tsaoling landslide triggered by the Chi–Chi earthquake, Taiwan: insights from a discrete element simulation. Eng Geol. 2009;106(1–2):1–19.
32. Lin C-H, Lin M-LL. Evolution of the large landslide induced by Typhoon Morakot: a case study in the Butangbunasi River, southern Taiwan using the discrete element method. Eng Geol. 2015;197:172–87.
33. Li WC, Li HJ, Dai FC, Lee LM. Discrete element modeling of a rainfall-induced flowslide. Eng Geol. 2012;149:22–34.
34. Sizkow SF, Usama ES. SPH-DEM simulations of saturated granular soils liquefaction incorporating particles of irregular shape. Comput Geotech. 2021;134: 104060.
35. Pastor M, Haddad B, Sorbino G, Cuomo S, Drempetic V. A depth-integrated, coupled SPH model for flow-like landslides and related phenomena. Int J Numer Anal Methods Geomech. 2009;33(2):143–72.
36. Pastor M, Blanc T, Haddad B, Petrone S, Sanchez Morles M, Drempetic V, Issler D, Crosta G, Cascini L, Sorbino G, Cuomo S. Application of a SPH depth-integrated model to landslide run-out analysis. Landslides. 2014;11(5):793–812.
37. Bui HH, Fukagawa R. An improved SPH method for saturated soils and its application to investigate the mechanisms of embankment failure: case of hydrostatic pore-water pressure. Int J Numer Anal Methods Geomech. 2013;37(1):31–50.
38. Zhang W, Maeda K, Saito H, Li Z, Huang Y. Numerical analysis on seepage failures of dike due to water level-up and rainfall using a water–soil-coupled smoothed particle hydrodynamics model. Acta Geotech. 2016;11(6):1401–18.
39. Swegle JW, Hicks DL, Attaway SW. Smoothed particle hydrodynamics stability analysis. J Comput Phys. 1995;116(1):123–34.
40. Libersky L, Randles P. Smoothed particle hydrodynamics: some recent improvements and applications. Comput Methods Appl Mech Eng. 1996;139(1):375–408.
41. Monaghan JJ. SPH without a tensile instability. J Comput Phys. 2000;159(2):290–311.
42. Liu WK, Jun S, Zhang YF. Reproducing kernel particle methods. Int J Numer Methods Fluids. 1995;20(8–9):1081–106.
43. Liu WK, Jun S, Li S, Adee J, Belytschko T. Reproducing kernel particle methods for structural dynamics. Int J Numer Methods Eng. 1995;38(10):1655–79.
44. Chen J-S, Pan C, Wu C, Liu WK. Reproducing kernel particle methods for large deformation analysis of nonlinear structures. Comput Methods Appl Mech Eng. 1996;139(1–4):195–227.
45. Jun S, Im S. Multiple-scale meshfree adaptivity for the simulation of adiabatic shear band formation. Comput Mech. 2000;25(2):257–66.
46. You Y, Chen J-S, Lu H. Filters, reproducing kernel, and adaptive meshfree method. Comput Mech. 2003;31(3):316–26.
47. Rabczuk T, Belytschko T. Adaptivity for structured meshfree particle methods in 2D and 3D. Int J Numer Methods Eng. 2005;63(11):1559–82.
48. Wu C-T, Hu W, Wang H-P, Lu H. A robust numerical procedure for the thermomechanical flow simulation of friction stir welding process using an adaptive element-free Galerkin method. Math Probl Eng. 2015;2015: 486346.
49. Chi S-W, Lee C-H, Chen J-S, Guan P-C. A level set enhanced natural kernel contact algorithm for impact and penetration modeling. Int J Numer Methods Eng. 2015;102(3–4):839–66.
50. Chen J-S, Pan C, Wu C. Large deformation analysis of rubber based on a reproducing kernel particle method. Comput Mech. 1997;19(3):211–27.
51. Chen J-S, Pan C, Roque CMOL, Wang H-P. A Lagrangian reproducing kernel particle method for metal forming analysis. Comput Mech. 1998;22(3):289–307.
52. Wei H, Chen J-S. A damage particle method for smeared modeling of brittle fracture. Int J Multiscale Comput Eng. 2018;16(4):303–24.
53. Guan P-C, Chi S-W, Chen J-S, Slawson TR, Roth MJ. Semi-Lagrangian reproducing kernel particle method for fragment-impact problems. Int J Impact Eng. 2011;38(12):1033–47.
54. Sherburn JA, Roth MJ, Chen J-S, Hillman M. Meshfree modeling of concrete slab perforation using a reproducing kernel particle impact and penetration formulation. Int J Impact Eng. 2015;86:96–110.
55. Yreux E. Generalized reproducing kernel particle method for fragment-impact and fracture modeling. San Diego: University of California; 2015.
56. Chen J-S, Wu Y. Stability in Lagrangian and semi-Lagrangian reproducing kernel discretizations using nodal integration in nonlinear solid mechanics. In: Computational methods in applied sciences. Dordrecht: Springer; 2007.
57. Guan PC, Chen J-S, Wu Y, Teng H, Gaidos JG, Hofstetter K, Alsaleh MI. Semi-Lagrangian reproducing kernel formulation and application to modeling earth moving operations. Mech Mater. 2009;41(6):670–83.
58. Chen J-S, Chi S-W, Lee C-H, Lin S-P, Marodon C, Roth MJ, Slawson TR. A multiscale meshfree approach for modeling fragment penetration into ultra high-strength concrete. Vicksburg: US Army Engineer Research and Development Center; 2011.
59. Wei H, Chen J-S, Beckwith F, Baek J. A naturally stabilized semi-Lagrangian meshfree formulation for multiphase porous media with application to landslide modeling. J Eng Mech. 2020;146(4):04020012.
60. Kwok O-LA, Guan P-C, Cheng W-P, Sun C-T. Semi-Lagrangian reproducing kernel particle method for slope stability analysis and post-failure simulation. KSCE J Civ Eng. 2015;19(1):107–15.
61. Reedlunn B, Moutsanidis G, Baek J, Huang T-H, Koester J, Matteo E, He X, Taneja K, Wei H, Bazilevs Y, Chen J-S, Mitchell C, Lander R, Dewers T. Initial simulations of empty room collapse and reconsolidation at the waste isolation pilot plant. Albuquerque: Sandia National Laboratories; 2019.
62. Pasetto M, Baek J, Chen J-S, Wei H, Sherburn JA, Roth MJ. A Lagrangian/semi-Lagrangian coupling approach for accelerated meshfree modelling of extreme deformation problems. Comput Methods Appl Mech Eng. 2021;381: 113827.

63. Belytschko T, Organ D, Krongauz Y. A coupled finite element-element-free Galerkin method. Comput Mech. 1995;17(3):186–95.
64. Brezzi F, Fortin M. Mixed and hybrid finite element methods. New York: Springer; 1991.
65. Chen J-S, Pan C. A pressure projection method for nearly incompressible rubber hyperelasticity, part I: theory. J Appl Mech. 1996;63(4):862–8.
66. Chen J-S, Wu C-T, Pan C. A pressure projection method for nearly incompressible rubber hyperelasticity, part II: applications. J Appl Mech. 1996;63(4):869–76.
67. Wei H, Chen J-S, Hillman M. A stabilized nodally integrated meshfree formulation for fully coupled hydro-mechanical analysis of fluid-saturated porous media. Comput Fluids. 2016;141:105–15.
68. Zienkiewicz OC, Xie Y, Schrefler B, Ledesma A, Bičanič N. Static and dynamic behaviour of soils: a rational approach to quantitative solutions. II. Semi-saturated problems. Proc R Soc Lond A Math Phys Sci. 1990;429(1877):311–21.
69. Zienkiewicz OC, Chan A, Pastor M, Schrefler B, Shiomi T. Computational geomechanics, vol. 613. Chichester: Wiley; 1999.
70. Meroi EA, Schrefler BA, Zienkiewicz OC. Large strain static and dynamic semisaturated soil behaviour. Int J Numer Anal Methods Geomech. 1995;19(2):81–106.
71. van Genuchten MT. A closed-form equation for predicting the hydraulic conductivity of unsaturated soils. Soil Sci Soc Am J. 1980;44(5):892–8.
72. Bochev PB, Dohrmann CR, Gunzburger MD. Stabilization of low-order mixed finite elements for the stokes equations. SIAM J Numer Anal. 2006;44(1):82–101.
73. White JA, Borja RI. Stabilized low-order finite elements for coupled solid-deformation/fluid-diffusion and their application to fault zone transients. Comput Methods Appl Mech Eng. 2008;197(49–50):4353–66.
74. Sun W, Ostien JT, Salinger AG. A stabilized assumed deformation gradient finite element formulation for strongly coupled poromechanical simulations at finite strain. Int J Numer Anal Methods Geomech. 2013;37(16):2755–88.
75. Belytschko T, Chen J-S, Hillman M. Meshfree and particle methods. Hoboken: Wiley Publishing Company; forthcoming.
76. Yreux E, Chen J-S. A quasi-linear reproducing kernel particle method. Int J Numer Methods Eng. 2017;109(7):1045–64.
77. Siriaksorn T, Chi S-W, Foster C, Mahdavi A. u-p semi-Lagrangian reproducing formulation for landslide modeling. Int J Numer Anal Methods Geomech. 2018;42(2):231–55.
78. Chen J-S, Wu C, Yoon S, You Y. A stabilized conforming nodal integration for Galerkin mesh-free methods. Int J Numer Methods Eng. 2001;50(1):435–66.
79. Chen J-S, Hillman M, Rüter M. An arbitrary order variationally consistent integration for Galerkin meshfree methods. Int J Numer Methods Eng. 2013;95(5):387–418.
80. Chen J-S, Hu W, Puso MA, Wu Y, Zhang X. Strain smoothing for stabilization and regularization of Galerkin meshfree method. In: Meshfree methods for partial differential equations III, vol. 57. Berlin: Springer; 2007. p. 57–76.
81. Puso MA, Chen J-S, Zywicz E, Elmer W. Meshfree and finite element nodal integration methods. Int J Numer Methods Eng. 2008;74(3):416–46.
82. Hillman M, Chen J-S. An accelerated, convergent, and stable nodal integration in Galerkin meshfree methods for linear and nonlinear mechanics. Int J Numer Methods Eng. 2016;107(7):603–30.
83. Li S, Liu WK. Reproducing kernel hierarchical partition of unity, part I—formulation and theory. Int J Numer Methods Eng. 1999;45(3):251–88.
84. Li S, Liu WK. Reproducing kernel hierarchical partition of unity, part II—applications. Int J Numer Methods Eng. 1999;45(3):289–317.
85. Chen J-S, Zhang X, Belytschko T. An implicit gradient model by a reproducing kernel strain regularization in strain localization problems. Comput Methods Appl Mech Eng. 2004;193(27–29):2827–44.
86. Soares D Jr. Iterative analysis of pore-dynamic models discretized by finite elements. Int J Numer Anal Methods Geomech. 2014;38(4):391–405.
87. Bui HH, Fukagawa R, Sako K, Ohno S. Lagrangian meshfree particles method (SPH) for large deformation and failure flows of geomaterial using elastic–plastic soil constitutive model. Int J Numer Anal Methods Geomech. 2008;32(12):1537–70.
88. Iseno H, Kohashi H, Furumoto K, Mori H, Ohno M. Large model tests of levee reinforcement method with toe drain for seepage failure. In: Proceedings of the annual symposium of Japanese geotechnical society, Tokyo; 2004.
89. Mori H. The SPH method to simulate river levee failures. Cambridge: University of Cambridge; 2008.
90. Mori H, Fukuhara N, Hattori A, Kuwano R, Soga K, Saito Y, Sasaki T. The SPH method for simulating the progressive sliding failure of a River Levee. Jpn Geotech J. 2014;9(4):687–96.
91. Khoei AR, Mohammadnejad T. Numerical modeling of multiphase fluid flow in deforming porous media: a comparison between two- and three-phase models for seismic analysis of earth and rockfill dams. Comput Geotech. 2011;38(2):142–66.

Publisher's Note